Check for updates

ADVANCING EARTH AND SPACE SCIENCE

Paleoceanography and Paleoclimatology

RESEARCH ARTICLE
10.1029/2020PA004116

Key Points:
- Cyclostratigraphy applied to two Eocene Indian Ocean scientific drilling records reveals the fingerprint of orbital eccentricity
- Sedimentary noise at both sites contains a 1.2-Myr obliquity imprint, albeit in antiphase: Mechanisms causing noise are thus different
- While sea-level change causes noise at shallower sites, bottom current intensity might introduce sedimentary noise at deep-ocean sites

Supporting Information:
- Supporting Information S1

Correspondence to:
K. Xu,
xuke@cug.edu.cn

Citation:
Xu, K., De Vleeschouwer, D., Vahlenkamp, M., Yang, R., & Chen, H. (2021). Reconstructing Eocene Eastern Indian Ocean dynamics using ocean-drilling stratigraphic records. *Paleoceanography and Paleoclimatology*, *36*, e2020PA004116. https://doi.org/10.1029/2020PA004116

Received 9 SEP 2020
Accepted 21 JAN 2021

© 2021. The Authors.
This is an open access article under the terms of the Creative Commons Attribution-NonCommercial License, which permits use, distribution and reproduction in any medium, provided the original work is properly cited and is not used for commercial purposes.

Reconstructing Eocene Eastern Indian Ocean Dynamics Using Ocean-Drilling Stratigraphic Records

Ke Xu[1,2], David De Vleeschouwer[2], Maximilian Vahlenkamp[2], Renchao Yang[3], and Honghan Chen[1]

[1]Faculty of Earth Resources, Key Laboratory of Tectonics and Petroleum Resource, Ministry of Education, China University of Geosciences, Wuhan, China, [2]MARUM—Center for Marine and Environmental Sciences, University of Bremen, Bremen, Germany, [3]Shandong Provincial Key Laboratory of Depositional Mineralization & Sedimentary Minerals, Shandong University of Science and Technology, Qingdao, China

Abstract The Eocene Epoch corresponds to the runup toward the Greenhouse to Icehouse Cenozoic transition. To fully appreciate this climate evolution, detailed and accurate age-depth models are required. While much progress has been made recently in the field of Eocene astrochronology, the construction of unambiguous Eocene astronomical timescales (ATS) is hampered by lithologically undetected hiatuses, the scarcity of carbonate-rich marine successions, and conflicting cyclostratigraphies. In this study, we present an orbital-scale cyclostratigraphy for Ocean Drilling Program (ODP) Hole 762C, and we reconstruct Eastern Indian Ocean dynamics. This reconstruction is based on two ocean-drilling Eocene sequences: ODP Hole 762C and International Ocean Discovery Program (IODP) Site U1514. Our eccentricity-based cyclostratigraphy for Hole 762C is integrated with existing bio and magnetostratigraphies and constitutes the most precise available chronology for this legacy site. The Hole 762C stratigraphy is combined with the existing Site U1514 age-depth model to obtain a high-resolution Eocene ATS for the Eastern Indian Ocean. We apply sedimentary noise modeling to obtain new insights in benthic turbulence at both sites. Despite the significant difference in paleo-waterdepth, noise levels at both sites carry a 1.2-Myr obliquity amplitude imprint. We interpret the sedimentary noise at Hole 762C, on a submarine plateau, in terms of sea-level change. The sedimentary noise at U1514, by contrary, is interpreted to be modulated by bottom current intensity as this site represents a deep-sea basinal environment. We conclude that, despite very similar astronomical signatures, the mechanistic pathways between astronomical forcing and sedimentary response were radically different at these two sites.

1. Introduction

The Eocene Epoch is a 22 Myr long geologic time slice that is chiefly characterized by a long-term cooling trend, ultimately leading up to the transition from the greenhouse to the icehouse Cenozoic climate state. The Eocene starts with the Paleocene-Eocene Thermal Maximum (PETM, ∼56 Ma), a rapid carbon cycle perturbation that resulted in a ∼5°C global average temperature rise (Norris & Röhl, 1999; Tripati & Elderfield, 2005; Zeebe & Lourens, 2019). The PETM is followed by a series of similarly short-lived hyperthermals, albeit of smaller amplitude. Around 40 Ma, the Middle Eocene Climate Optimum (MECO, ∼40 Ma) unfolded as a somewhat longer hyperthermal with a ∼4°C increase in surface and ocean temperatures (Bohaty & Zachos, 2003; Bohaty et al., 2009; Boscolo Galazzo et al., 2014; Edgar et al., 2010; Sluijs et al., 2013; Westerhold & Röhl, 2013). Finally, the Eocene-Oligocene transition (EOT, ∼34 Ma) constitutes a climatic shift characterized by global cooling, decreasing atmospheric CO_2, oceanographic reorganization and the appearance of substantial ice sheets on Antarctica (Coxall & Pearson, 2007; Hren et al., 2013; Westerhold et al., 2014; Zachos et al., 2001, 2008).

The scarcity of continental ice throughout the Eocene caused ice-related positive feedback mechanisms to be subdued during this Epoch. Nevertheless, several studies found a distinct Eocene climate response to astronomical Milankovitch forcing (Boulila et al., 2018; Jovane et al., 2010; Vahlenkamp et al., 2020a). The insignificance of ice-related climate feedback mechanisms makes that the Eocene climate state was characterized by a fundamentally different response to astronomical insolation forcing compared to the much-studied Pleistocene glacial-interglacial cycles. A mechanistic understanding of this state-specific climate response to astronomical forcing is still a scientific frontier in paleoclimatology (Keery et al., 2018;

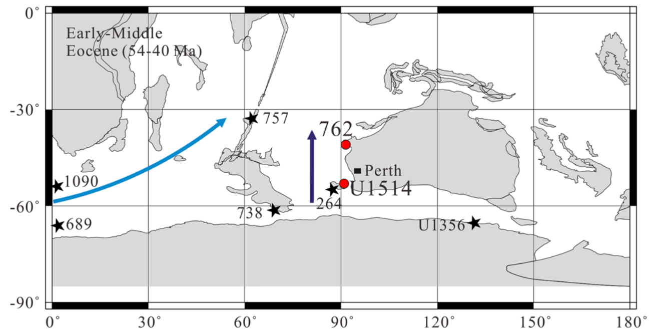

Figure 1. Location of Hole 762C and Site U1514 used for timescale reconstruction in the Eocene. Simplified deep water mass circulation in the Southern Ocean during early to middle Eocene in this study (after Huck et al., 2017). Dark blue arrow represents deep water formation around Antarctica flowing to the Indian Ocean. Light blue arrow represents deep water formation in the Atlantic sector of the Southern Ocean flowing to the Indian Ocean. (paleogeographic map, www.odsn.de).

Lunt et al., 2020). The astronomical Milankovitch cycles induce oscillations in the insolation distribution across latitudes and seasons on 10^4–10^6 year timescales. This insolation variability has an important impact on climate, and these astronomically forced climate oscillations can in turn be documented in climate-sensitive sedimentary archives (Hinnov, 2013; Hinnov & Hilgen, 2012; Strasser et al., 2006). The combination of such climate cycles in sedimentary sequences with biostratigraphy, radio-isotopic dating or magnetostratigraphy, has the potential to yield high-resolution astronomically constraint age-depth models (so-called astrochronologies). For the Neogene, this technique enabled the construction of a fully astronomically tuned Geological Time Scale (GTS) (GTS2012, Gradstein et al., 2012). Astronomical tuning has been a popular method for Eocene sedimentary sequences as well and considerable progress has been made in the construction of an Astronomical Time Scale (ATS) for the Eocene Epoch (Boulila et al., 2018; Dinarès-Turell et al., 2018; Francescone et al., 2019; Jovane et al., 2010; Kodama et al., 2010; Lourens et al., 2005; Pälike et al., 2001; Vahlenkamp et al., 2020a; Westerhold & Röhl 2009, 2013; Westerhold et al., 2007, 2014, 2015). However, the occurrence of hiatuses, the scarcity of Eocene carbonate-rich marine successions, and different interpretations among authors hampers the construction of an unambiguous astronomically constrainted Eocene GTS. This, in turn, complicates a comprehensive and process-level understanding of Eocene climate and ocean dynamics.

Reconstructing global sea-level changes (GSLC) for the Cenozoic is another challenging issue. Two methods are primarily used for reconstructing GSLC. The most elemental method is sequence stratigraphy, which uses the identification of sequence boundaries to reconstruct GSLC. Vail et al. (1977) proposed that Phanerozoic GSLC could be reconstructed by synthesizing the relative sea level changes from different sites. However, the original materials used to reconstruct GSLC are often not disclosed, which makes it difficult for other scholars to evaluate the reliability of GSLC obtained by this method (Catuneanu et al., 2009). Another method to reconstruct GSLC relies on foraminiferal calcite oxygen isotopes ($\delta^{18}O$) (Miller et al., 2005). Miller et al. (2020) combined "backstripping" methods and Pacific benthic foraminiferal $\delta^{18}O$ and Mg/Ca records to reconstruct a high-resolution GSLC for the entire Cenozoic. Recently, a third method called sedimentary noise modeling has been proposed for GSLC reconstructions. This technique analyses the dynamics of the nonorbital signal component of climate indicator data (a so-called climate proxy) to reconstruct GSLC from continental margin sequences (Li et al., 2018). The principle of this techniques relies on the assumption that the sedimentary noise level in continental margin sections decreases when sea level rises, and vice versa.

To date, sedimentary noise modeling has not yet been attempted at deep-ocean basinal sites. In this study, we will apply this technique to a deep ocean-drilling archive from the Mentelle Basin (3,850 m water depth) and advocate that bottom-water current intensity rather than sea-level change determines sedimentary noise at this abyssal depth. In fact, we present a latitudinal transect of two ocean-drilling Eocene sequences from the Eastern Indian Ocean. Ocean Drilling Program (ODP) Hole 762C on the Exmouth Plateau (1,360 m water depth) constitutes the northern end-member in this study. The Eocene sequences of International Ocean Discovery Program (IODP) Site U1514 in the Mentelle Basin (3,850 m water depth) are located in the southeastern Indian Ocean (Figure 1). The goals of this study are (1) to combine an astrochronologic approach based on downhole logging records from Hole 762C with existing bio and magnetostratigraphies to obtain a high-resolution and accurate age-depth model; (2) to construct a regional high-resolution Eocene ATS for the Eastern Indian Ocean, integrating the Hole 762C chronology with the existing astrochronology for Site U1514; and (3) to apply the sedimentary noise modeling technique to both sites and to compare their results to the recent GSLC reconstruction by Miller et al. (2020).

2. Materials and Methods

2.1. Ocean-Drilling Archives

Hole 762C (19°53.23′S, 112°15.24′E) is located on the western part of the central Exmouth Plateau (northern Carnarvon Basin) at a present-day water depth of 1,360 m (Figure 1) (Haq et al., 1990). The Cenozoic sedimentary environment corresponds to an open-ocean setting that has been tectonically quiescent since the mid-Cretaceous (Haq et al., 1992). A detailed cyclostratigraphic age-depth model has been recently constructed for the Plio-Pleistocene (Auer et al., 2020; Stuut et al, 2019). The Eocene portion of Hole 762C consists of 242-m-thick (180–422 m below sea floor [mbsf]) carbonate sediments that were deposition above the carbonate compensation depth (CCD) (Shamrock & Watkins, 2012). This interval has been divided into three lithologic subunits: the ∼180–265 mbsf interval consists of white nannofossil chalk; the ∼265–398 mbsf interval consists of light green-gray and white nannofossil chalk with foraminifera; the ∼398–422 mbsf interval consists of light green nannofossil chalk with foraminifera (Haq et al., 1992). Shamrock et al. (2012) identified four major hiatuses in Hole 762C Eocene interval based on the stratigraphic cross-correlation of planktonic foraminiferal and calcareous nannofossil biostratigraphy, magnetostratigraphic reversals, as well as bulk stable isotope excursions. Hiatuses are reported at 289.75, 321.13, 332.18, and 412.78 mbsf and represent between ∼0.9 and 2.2 Myr of missing time. These authors attribute the hiatuses to nondeposition rather than to erosion, but are not more specific as to which mechanism is ultimately responsible for the reported disconformities. While additional minor hiatuses cannot be fully excluded, the integrated approach adopted in Shamrock et al. (2012) provides a robust stratigraphic framework on which we build in this study. Since there are no lithological or stratigraphic indications for additional gaps, we assume continuous sedimentation in-between the reported hiatuses and our cyclostratigraphic analysis is organized according.

Site U1514 (33°7.2443′S, 113°5.4799′E) is located in the northernmost Mentelle Basin at 3,850 m waterdepth (Figure 1) (Huber et al., 2019). Its great paleodepth and high paleolatitude (∼60°S in at 50 Ma) make Site U1514 an interesting site to study changes in climate and deep ocean circulation, during the final phase of breakup of the Gondwana continents. The lower to middle Eocene interval section consists of lighter greenish gray clayey nannofossil chalk and darker nannofossil-rich claystone (Huber et al., 2019). In this study, we adopt the U1514 lower to middle Eocene astronomical time scale as constructed by Vahlenkamp et al. (2020a).

2.2. Th/K Ratio Quantified from Wireline-Logging Natural Gamma Radiation Spectra

Downhole wireline logging with a natural gamma radiation (NGR) spectrometer provides elemental data of potassium (K), thorium (Th) and Uranium (U). The K component of the signal is mainly associated with feldspar, micas, clays, and salts. The host minerals for Th are typically clays, feldspars, heavy minerals, and phosphates (Schnyder et al., 2006). A Miocene study that involved IODP Site U1459 in the eastern Indian Ocean (Groeneveld et al., 2017) advocates Th/K as a proxy for humid versus dry conditions. An increase in K would indicate an enhanced siliciclastic sediment flux in response to more humid conditions in southwestern Australia. Thorium, on the other hand, mainly resides in heavy minerals that are mainly wind-transported (Kuhnt et al., 2015). A Pliocene study by De Vleeschouwer et al. (2019) associates minima in K/Al at Site U1459 with more arid intervals and more eolian transport. These authors thus adopt a proxy interpretation that is congruent with Groeneveld et al. (2017) in terms of the potassium proxy response to hydroclimate change. In this Eocene study, we comply with these earlier proxy interpretations at nearby Site U1459, as we associate high Th/K with dry conditions in southwest Australia, and low Th/K with wetter conditions.

There are two reasons why Th/K can be a good recorder of astronomically forced climate signals. First, astronomical insolation forcing can directly influence the hydrological cycle over western Australia and thus cause oscillations between more arid and more humid conditions paced by the rhythms of eccentricity-modulated precession or obliquity. High eccentricity increases the amplitude of the precessional cycle, which means that seasonal extremes could be intensified. Enhanced seasonality would in turn have an influence on the summer precipitation. More riverine input and higher amounts of rainfall would result in high K values and thus low Th/K values, and vice versa. Second, sea-level changes would affect relative influxes of clays and carbonate. We thus conclude that Th/K could be used as a paleoclimate proxy in the Eastern Indian Ocean. We note, however, that some authors raised concerns about Th/K as a paleoclimate proxy in carbonate-rich marine successions (Ghasemi-Nejad et al., 2015; Li, Huang, et al., 2019). Yet, their conclusions are specific to the hinterland in the studied areas. The highly sensitive hydrological cycle in

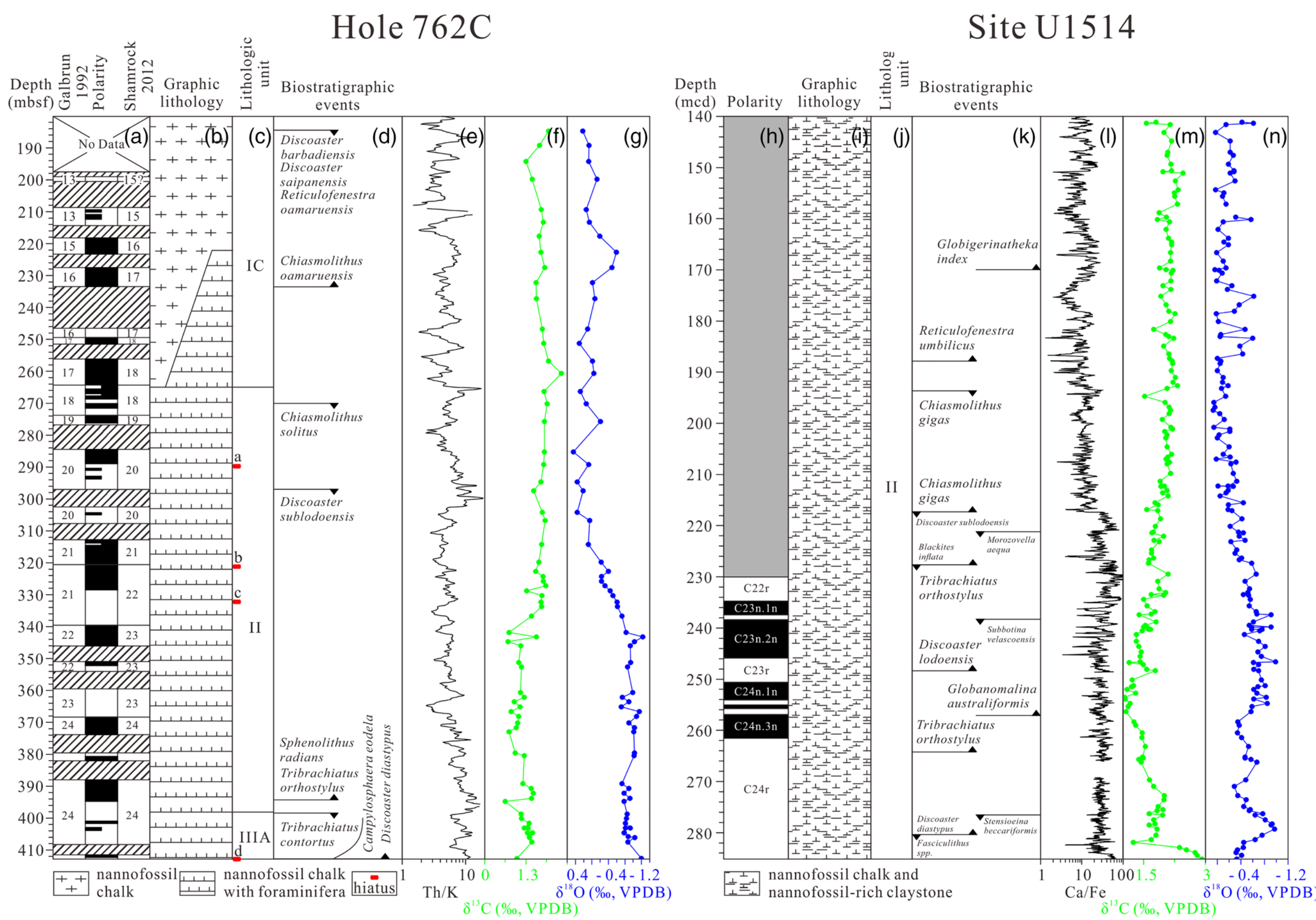

Figure 2. (a) Magnetostratigraphy of Galbrun (1992) and Shamrock et al. (2012), white = reversed, black = normal, hatchmarks = no core recovery. (b) Lithologic column for Site 762C. (c) Lithologic unit and hiatuses. Unit IC = the ~180–265 mbsf interval consists of white nannofossil chalk; Unit II = ~265–398 mbsf interval consists of light green-gray and white nannofossil chalk with foraminifera; Unit III = ~398–422 mbsf interval consists of light green nannofossil chalk with foraminifera (Haq et al., 1992). Hiatuses are reported at 289.75 mbsf (a), 321.13 mbsf (b), 332.18 mbsf (c) and 412.78 mbsf (d) by red thick line (Shamrock et al., 2012).(d) Biostratigraphic events (Shamrock et al., 2012). (e) Th/K of Hole 762C. (f)–(g) Bulk sediment carbon and oxygen isotope data of Hole 762C. (h) Magnetostratigraphic interpretation for Site U1514 (white = reversed, black = normal, gray = undetermined) (Vahlenkamp et al., 2020a). (i) Lithologic column for Site U1514. (j) Lithologic unit. Unit II = lighter greenish gray clayey nannofossil chalk and darker nannofossil-rich claystone (Huber et al., 2019). (k) Biostratigraphic events (Huber et al., 2019). (L) Ca/Fe from U1514. (M–N) Bulk sediment carbon and oxygen isotope data of U1514.

southwest Australia combined with the successful use of the Th/K proxy in previous studies, lead us to conclude that Th/K is well-suited for the analysis of orbital frequencies possibly imprinted in the sedimentary archives studied here.

2.3. Biostratigraphy and Magnetostratigraphy

The calcareous nannofossil biostratigraphy of Hole 762C was initially constructed by Siesser and Bralower (1992), and later revised by Shamrock and Watkins (2012). The latter authors analyzed 187 samples at 0.75 m intervals to significantly increase the precision of key biostratigraphic markers (Figure 2d). The Eocene magnetostratigraphy of Hole 762C was provided by ODP 122 Scientific Results (Galbrun, 1992) (Figure 2a). However, poor core recovery in some intervals led to ambiguous interpretations. The original age-depth model was based on magnetostratigraphic results which referred to the calcareous nannofossil biostratigraphy (Berggren et al., 1995). Later, several issues with the original age-depth model were highlighted as Shamrock et al. (2012) identified four hiatuses based on refined biostratigraphic markers. Based on this new information, these authors revised the magnetostratigraphic interpretations (Figure 2a).

2.4. Bulk Sediment Carbon and Oxygen Isotopes

The bulk sediment carbon and oxygen isotopes of Hole 762C (Figures 2f and 2g) with an average sampling interval of 3.4 m were provided by ODP 122 Scientific Results (Thomas et al., 1992). The bulk sediment carbon and oxygen isotopes of U1514 (Figures 2m and 2n) with an average sampling interval of 0.9 m were published in Vahlenkamp et al. (2020a, 2020b).

2.5. Time Series Analyses

The 762C downhole logging Th/K depth-series was first converted using a $\log_{10}$ transformation to attenuate nonstationary features in the raw data (Weedon, 2003). The $\log_{10}$(Th/K) data contained a handful outliers (N = 16; with $\log_{10}$(Th/K) > 0.173 and <1.275 considered as outliers), which were removed prior to time series analysis (Figure 2e). For the analysis, we divided the $\log_{10}$(Th/K) series into four intervals: (1) 180–289.75 m, (2) 289.75–321.13 m, (3) 321.13–332.18 m, and (4) 332.18–412.78 m with breaks corresponding to the hiatuses identified by Shamrock et al. (2012). The third depth interval contains ~11 m of sediment, and considering that Shamrock et al. (2012) report average sedimentation rate estimates for the interval between ~1 and ~2 cm/kyr, we considered this interval too short to be analyzed with confidence.

To remove low-frequency long-term trends and highlight astronomical signals for each interval, the $\log_{10}$(Th/K) series were detrended by subtracting corresponding weighted averages using the LOWESS method (Cleveland, 1979). We then used a sliding-window evolutionary Fast Fourier transform (FFT) spectrogram approach to identify the changing frequencies of the $\log_{10}$(Th/K) series due to variable sedimentation rate in an evolutive power spectrum (Kodama & Hinnov, 2014). The $\log_{10}$(Th/K) series were analyzed by 2π multitaper method (MTM) spectral estimator (Thomson, 1982), estimated spectra in MTM were compared to robust red noise models (Mann & Lees, 1996). Gaussian bandpass filtering was performed to extract the eccentricity cycles in the $\log_{10}$(Th/K) series. We used 405-kyr long-eccentricity cycles for astronomical calibration as this eccentricity component is the most stable orbital parameter throughout the Phanerozoic (Hinnov & Hilgen, 2012; Laskar et al., 2004). Moreover, the 405-kyr eccentricity metronome can be used for astronomical tuning in the Eocene. Hence, in a last step, we tuned the 405-kyr component in the $\log_{10}$(Th/K) series to the La2010c astronomical solution (Laskar et al., 2011). The La2010c eccentricity solution is used in this study, as it is the solution with the lowest Root Mean Square Deviation with respect to Eocene cyclostratigraphic results by Westerhold et al. (2017) and Vahlenkamp et al. (2020a), while the ZB18a solution turned out to provide an even beter fit in Zeebe and Lourens (2019). The choice of eccentricity solution becomes relevant when going back in time beyond 50 Ma, as eccentricity solutions start to disagree on the phasing and amplitude of the 100-kyr rhythm. All above steps were done using Acycle v2.1 software (Li, Hinnov, & Kump, 2019) and are documented in the Supporting Information (Supporting Text S1–S4, Supporting Figures S1–S14, Supporting Table S1).

2.6. Sedimentary Noise Modeling

Li et al. (2018) introduced a sedimentary noise model for astronomically forced marginal marine successions as a means to reconstruct and evaluate sea-level changes. There are multiple sources for noise in the sedimentary climate signals. Noise sources that relate to climate and sea-level variability include water-depth related noise such as storms, tides and bioturbation. However, sedimentary noise can also be introduced by proxy sensitivity, measurement errors, nonlinear climate responses, and other factors such as dating errors, unstable depositional rates, tectonics, volcanism and diagenesis (Hinnov, 2013; Weedon, 2003). Among these noise sources, variations in the water-depth related noise at a fixed position in marginal marine successions have the potential to provide insights in relative sea-level changes. When sea level rises, water-depth related noise is assumed to decrease in response to a more stationary sedimentary environment, and vice versa. This model has been tested and applied to reconstruct Quaternary and Triassic sea-level changes in marine successions (Li et al., 2018). Whether it can be applied to Eocene ocean-drilling records from the Eastern Indian Ocean will be evaluated here.

The sedimentary noise model involves complementary approaches: dynamic noise after orbital tuning analysis (DYNOT), and lag-1 autocorrelation coefficient (ρ_1) analysis (Li et al., 2018). The DYNOT model was originally formulated to detect sea level variations in tuned marine cyclostratigraphy deposited at ocean depths near storm wave base. DYNOT sums the spectral power in frequency bands defined for the eccentricity, obliquity and precession index, and divides this sum by the total spectral power summed across all frequencies of the input time series. Subtracting this ratio from 1 gives the R, the proportion of power due to nonorbital, uncorrelated noise. When R is relatively high, sea level is relatively low (with a lower storm wave base more likely to disturb sedimentation), and vice versa. Thus, it can be used to measure noise in climate and sea-level proxies. The ρ_1 model is tested as a second, independent noise indicator for relative sea-level change (Li et al., 2018). The details of the calculation algorithm are presented in Li et al. (2018). When the algorithm estimates a low noise level, it will produce a low DYNOT value and a high ρ_1 value, which in turn is thought to be indicative of sea level high-stands, and vice versa. This model has been developed for slope and basin environments at water depths ranging from few meters to several hundred meters, which are near or just below storm-wave base. The two ocean drilling sites of this study correspond to very different paleo-water depths, including a submarine plateau (762C) and a deep-sea basinal environment (U1514). This manuscript thus constitutes the first case study in which the sedimentary noise model is applied to a sequence of contemporary sections with greater paleo-water-depths. The results of the sedimentary noise modeling are thus carefully evaluated and interpreted in light of the depositional environment.

3. Results

3.1. ODP Hole 762C

The $\log_{10}$(Th/K) depth-series displays rhythmical meter-scale variability, which we subject to cyclostratigraphic analysis. A low-resolution oxygen isotope (δ^{18}O) depth-series is available (Figure 2f). Despite the fact that this δ^{18}O data have been measured on bulk sediments and not on species-specific foraminifera, it reflects the multimillion-year cooling trend from the early Eocene into the late Eocene through the gradual increase in δ^{18}O.

3.1.1. Age Control and Astronomical Solution

The Shamrock et al. (2012) age-depth model for Hole 762C combines improved biostratigraphy with magnetostratigraphy, yet the poor core recovery and the four identified hiatuses hamper the development of an unequivocal chronostratigraphic framework. At the same time, the Shamrock et al. (2012) age model referred to the 2008 geomagnetic polarity timescale (GPTS 2008) that has time-offsets for Eocene chron-boundaries of up to ~1 Myr in comparison to GTS2012.

Our aim is to further improve the Hole 762C chronostratigraphic framework by adding cyclostratigraphic time constraints for distinct depth-intervals that are uninterrupted by major hiatuses. In each of the three studied depth-intervals, we anchor the floating cyclostratigraphy (relative time constraints only, therefore floating in absolute time) at the magnetochron boundary that is considered most reliable, and as far away as possible from an unconformity.

3.1.2. Astronomical Tuning of 762C

3.1.2.1. 180–289.75 m Interval

In the middle to upper Eocene interval of 762C, the evolutionary FFT spectrogram of the $\log_{10}$(Th/K) depth-series exhibits a frequency-band with elevated power around 0.16 m^{-1} (6.25 m wavelength) that is persistent throughout the interval with a local shift to slightly higher frequencies around 200 m (Figure 3c). The stability of this sedimentary rhythm confirms the indications from bio and magnetostratigraphy that sediment accumulation rate is relatively steady between 180 and 289.75 mbsf. The power spectrum of the $\log_{10}$(Th/K) depth-series (Figure 3d) substantiates a prominent ~6.23 m (0.1604 cycles/m) sedimentary

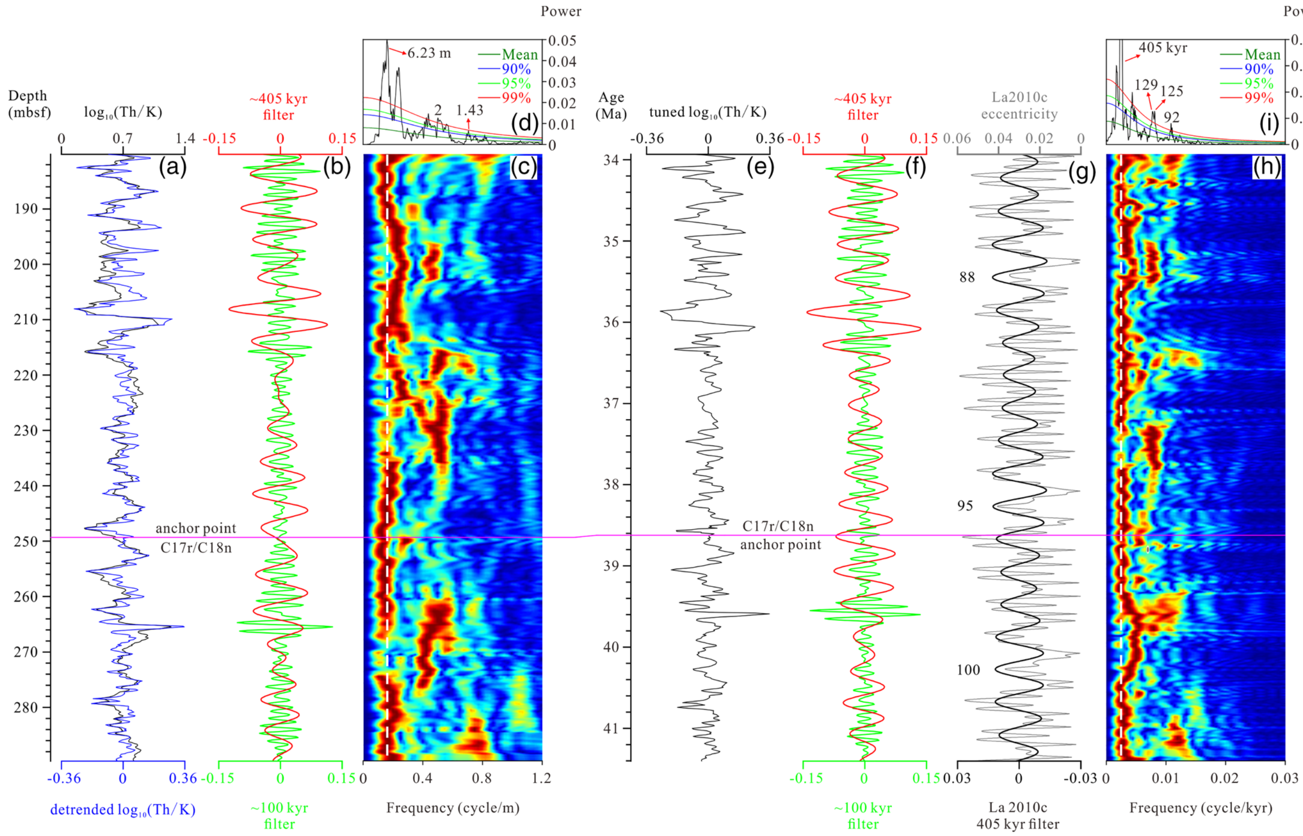

Figure 3. Cyclostratigraphic interpretation of 762C of 180–289.75 mbsf interval. (a) $\log_{10}$(Th/K) and detrended $\log_{10}$(Th/K) (after detrending by subtracting a 5.5% weighted average, 6.03 m) in the depth domain. (b) ~100-kyr filter (~1.43 m, passband is 0.7 ± 0.175 m^{-1}) and ~405-kyr filter (~5.88 m, passband is 0.17 ± 0.042 m^{-1}) of the detrended $\log_{10}$(Th/K) depth-series. (c) evolutionary FFT spectrogram of the $\log_{10}$(Th/K) depth-series (sliding window is 10 m with a step of 0.1524 m). (d) 2π MTM power spectrum of the $\log_{10}$(Th/K) depth-series. (e) tuned $\log_{10}$(Th/K) time-series. (f) ~100-kyr filter and ~405-kyr filter of the tuned $\log_{10}$(Th/K) time-series. (g) The La2010c eccentricity solution and its 405-kyr filters, the numbers on the eccentricity cycles indicate the position of the 2.4-Myr eccentricity nodes. (h) evolutionary FFT spectrogram of the $\log_{10}$(Th/K) time-series (sliding window is 500 kyr with a step of 10 kyr). (i) 2π MTM power spectrum of the $\log_{10}$(Th/K) time-series. The purple solid line represents the magnetostratrigraphic anchor point (C17r/C18n chron boundary, 249.41 mbsf, 38.615 Ma in GTS2012). FFT, Fast Fourier transform; MTM, multitaper method.

cycle, while also exhibiting spectral peaks at frequencies of 0.5 cycles/m (2 m) and 0.705 cycles/m (1.43 m), both exceeding the 99% confidence level. Shamrock et al. (2012) report average sedimentation rate estimates for this interval between ~1.1 and ~1.6 cm/kyr. Hence, in our working-hypothesis, we assigned the ~6.23 m cycles to the 405-kyr eccentricity cycle. These 405-kyr eccentricity cycles were bandpass filtered from the $\log_{10}$(Th/K) depth series (Gaussian bandpass filter between 0.128 and 0.212 cycles/m, equivalent to 4.72–7.81 m periodicities). The filtered signal yields 18 cycles. In a like manner, we bandpass filtered the 100-kyr eccentricity cycles from the $\log_{10}$(Th/K) depth-series (Gaussian bandpass filter between 0.525 and 0.875 cycles/m, equivalent to 1.14–1.9 m periodicities) and we obtain 77 cycles in the studied interval (Figure 3b).

We selected the C17r/C18n.1n chron boundary (249.41 mbsf, 38.615 Ma in GTS2012) as the anchor point for the floating cyclostratigraphy for this interval. Working from this age-depth anchor, we adopted a 405-kyr eccentricity tuning method to obtain an ATS for this interval. The power spectrum of the tuned $\log_{10}$(Th/K) time-series (Figure 3i) exhibits prominent peaks at periodicities of 405 kyr, 129, 125, and 92 kyr. In other words, our minimal 405-kyr tuning approach leads to elevated power at ~100-kyr eccentricity frequencies. This 100-kyr power has not been imposed by the tuning approach and is therefore a supporting argument for the assumptions made during ATS construction. In the evolutionary power spectrum (Figure 3h) one can observe persistent power in the 405-kyr band, yet this power was inflicted by our tuning-strategy. Our cyclostratigraphy suggests a duration for this interval of 7.47 Myr.

10.1029/2020PA004116

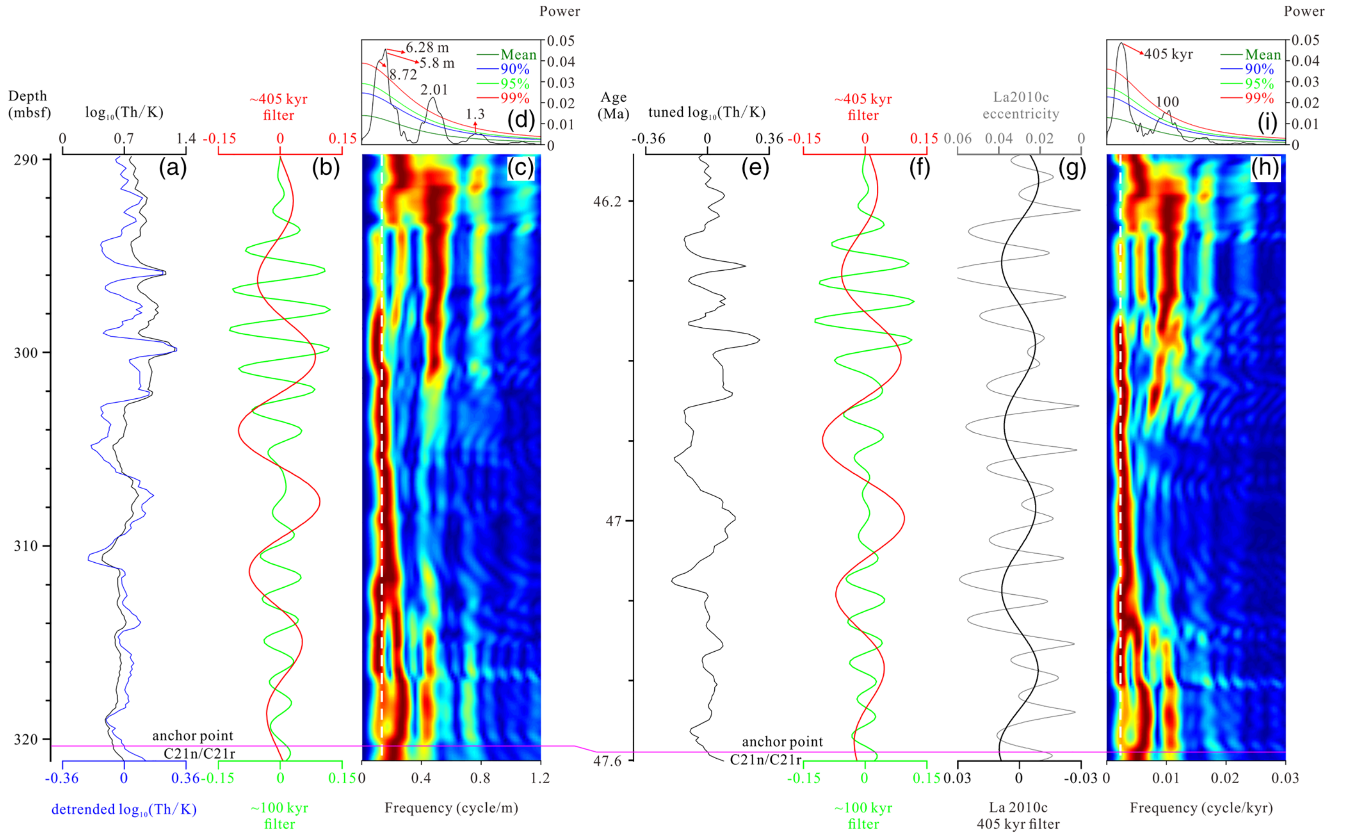

Figure 4. Cyclostratigraphic interpretation of 762C of 289.75–321.13 mbsf interval. (a) $\log_{10}$(Th/K) and detrended $\log_{10}$(Th/K) (after detrending by subtracting a 40% weighted average, 12.5 m) in the depth domain. (b) ~100-kyr filter (~2.12 m, passband is 0.47 ± 0.12 m^{-1}) and ~405-kyr filter (~7.69 m, passband is 0.13 ± 0.0325 m^{-1}) of the detrended $\log_{10}$(Th/K) depth-series. (c) evolutionary FFT spectrogram of the $\log_{10}$(Th/K) depth-series (sliding window is 12 m with a step of 0.1524 m). (d) 2π MTM power spectrum of the $\log_{10}$(Th/K) depth-series. (e) tuned $\log_{10}$(Th/K) time-series. (f) ~100 and ~405-kyr filter of the tuned $\log_{10}$(Th/K) time-series. (g) The La2010c eccentricity solution and its 405-kyr filter. (h) evolutionary FFT spectrogram of the $\log_{10}$(Th/K) time-series (sliding window is 500 kyr with a step of 5 kyr). (i) 2π MTM power spectrum of the $\log_{10}$(Th/K) time-series. The purple solid line represents the magnetostratigraphic anchor point (C21n/C21r chron boundary, 320.25 mbsf, 47.575 ± 0.018 Ma in Westerhold et al., 2015). FFT, Fast Fourier transform; MTM, multitaper method.

3.1.2.2. 289.75–321.13 m Interval

The evolutionary FFT spectrogram (Figure 4c) of the $\log_{10}$(Th/K) depth-series exhibits persistent high power at frequencies around 0.13 m^{-1} (7.69 m). The $\log_{10}$(Th/K) MTM spectrogram in the depth-series (Figure 4d) exhibits significant spectral peaks at wavelengths of ~8.72–5.8 m, 2.01 m, and 1.3 m (>99% confidence level). Bio and magnetostratigraphic constraints suggest an average sedimentation rate for this interval of ~1.1 cm/kyr (Shamrock et al., 2012), which implies that the observed 7.69 m cycle is too thick to be assigned to 405-kyr eccentricity. Despite this mismatch, we explore the working hypothesis that a ~7.69 m cycle represents a 405-kyr cycle. Under that assumption, to extract 405-kyr cycles from the $\log_{10}$(Th/K) depth-series, we adopted bandpass filtering between 0.0975 and 0.1625 cycles/m (equivalent to 6.15–10.25 m periodicities), yielding four cycles. Analogously, the assumed 100-kyr cycles were bandpass filtered (0.35–0.59 cycles/m passband, equivalent to 1.69–2.86 m periodicities), resulting in 15 cycles (Figure 4b).

We adopted the C21n/C21r chron boundary (320.25 mbsf, 47.575 ± 0.018 Ma in Westerhold et al., 2015) as the anchor point for this interval, as it was the only choice. The MTM power spectrum of the tuned $\log_{10}$(Th/K) time series (Figure 4i) obviously exhibits a spectral peak at 0.002469 cycles/kyr, as this peak was introduced by the cyclostratigraphic calibration process. The evolutionary FFT spectrogram (Figure 4h) indicates that the interpreted 405 and 100-kyr eccentricity are important components of the analyzed signal throughout. The stability of these frequencies within the time-domain, as well as the occurrence of ~100-kyr spectral peaks that are not induced by the tuning strategy, provide important arguments for the adopted working hypothesis and tuning assumptions. After tuning to the 405-kyr target curve, the interval under

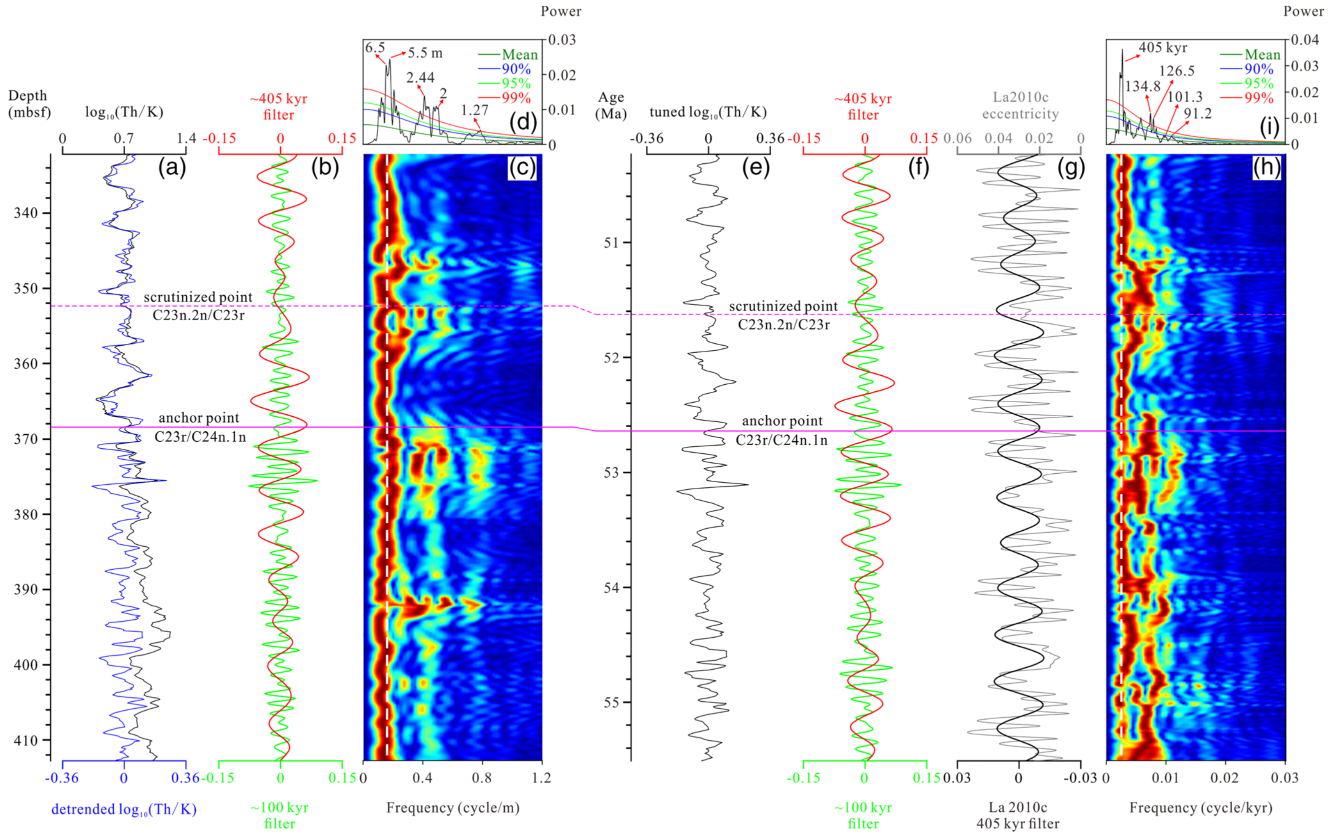

Figure 5. Cyclostratigraphic interpretation of 762C of 332.18–412.78 mbsf interval. (a) $\log_{10}$(Th/K) and detrended $\log_{10}$(Th/K) (subtraction of an 8 % weighted average, 6.44 m) in the depth domain. (b) ~100-kyr filters (~1.43 m, passband is 0.7 ± 0.175 m^{-1}) and ~405-kyr filters (~6.25 m, passband is 0.16 ± 0.04 m^{-1}) of the detrended $\log_{10}$(Th/K) depth-series. (c) evolutionary FFT spectrogram of the $\log_{10}$(Th/K) depth-series (sliding window is 10 m with a step of 0.1524 m). (d) 2π MTM power spectrum of the $\log_{10}$(Th/K) depth-series. (e) tuned $\log_{10}$(Th/K) time-series. (f) ~100 and ~405-kyr filters of the tuned $\log_{10}$(Th/K) time-series. (g) The La2010c eccentricity solution and its 405-kyr filters. (h) evolutionary FFT spectrogram of the $\log_{10}$(Th/K) time-series (sliding window is 500 kyr with a step of 10 kyr). (i) 2π MTM power spectrum of the $\log_{10}$(Th/K) time-series. The purple solid line represents the magnetostratigraphic anchor point (C23r/C24n.1n chron boundary, 368.31 mbsf, 52.628 ± 0.053 Ma in Westerhold et al., 2017), and the purple dashed line represents the scrutinized point (C23n.2n/C23r chron boundary, 352.22 mbsf, 51.737 ± 0.123 Ma in Westerhold et al., 2017). FFT, Fast Fourier transform; MTM, multitaper method.

investigation spans 1.52 Myr. In other words, we deduced an average sedimentation rate of ~1.9 cm/kyr for this interval, rather than ~1.1 cm/kyr as suggested by Shamrock et al. (2012). Possible reasons for the large discrepancy between both estimates reside with the multiple hiatuses, complicating the determination of reliable bio and magnetostratigraphic datums, as well as with the relatively short duration of this interval.

3.1.2.3. 332.18–412.78 m Interval

The evolutionary power spectra of the $\log_{10}$(Th/K) depth-series (Figure 5c) exhibits a dominant frequency around 0.164 m^{-1} (6.1 m). The $\log_{10}$(Th/K) MTM spectrogram in the depth series (Figure 5d) reveals noteworthy sedimentary cycles with wavelengths of ~6.5–5.5 m, ~2.44–2 m, and 1.27 m (>99% confidence level). The average sedimentation rates observed for this interval is ~2 cm/kyr (Shamrock et al., 2012). Hence, we associated the ~6.25 m cycles with the 405-kyr eccentricity cycle. We applied a bandpass filter (~6.25 m) between 0.12 and 0.2 cycles/m (equivalent to 5–8.3 m periodicities) bandpass to extract the 405-kyr cycles from the depth-series, yielding 13 cycles. To extract 100-kyr cycles from the depth-series, we adopted bandpass filtering (~1.43 m) between 0.525 and 0.875 cycles/m (equivalent to 1.14–1.9 m periodicities), resulting in 57 cycles (Figure 5b).

The C23r/C24n.1n chron boundary (368.31 mbsf, 52.628 ± 0.053 Ma, Westerhold et al., 2017) constitutes the anchor point for this interval. After 405-kyr minimal tuning, the power spectrum of the tuned $\log_{10}$(Th/K) time series (Figure 5i) indicates spectral peaks at periodicities of 405 kyr (the tuned period), 134.8, 126.5, 101.3, and 91.2 kyr. In the evolutionary FFT spectrogram (Figure 5h), one can observe persistent power in the 405-kyr band. After tuning to the 405-kyr target curve, the interval under investigation spans 5.28 Myr. In this interval, there is a second unambiguously identified chron boundary that can be used for further scrutinization of our cyclostratigraphy: In our tuning, the C23n.2n/C23r chron boundary (352.22 mbsf) was assigned an age of 51.626 Ma, which is consistent with the age estimates of Westerhold et al. (2017, 51.737 ± 0.123 Ma) and Francescone et al. (2019, 51.724 Ma). Thus, our ATS withstands this robustness test.

3.2. IODP Site U1514

Vahlenkamp et al. (2020a) split the Ca/Fe depth-series of U1514 into two intervals for analysis. The younger interval corresponds to the middle Eocene and ranges between ~142 and 203 mcd, the older interval is of early Eocene age and contains sediments between ~203 and 284 mcd. Both intervals are characterized by lithological alternations between light greenish gray chalk, and darker-colored chalk that is rich in clay (Huber et al., 2019). The lithological variability is thus accentuated by variations in color and CaCO3 content and occurs with a ~1 m rhythmicity. These authors also observe sediment layers that are particularly clay-rich and dark every 3–5 m. Average sedimentation rates throughout both intervals are about 0.95 cm/kyr, based on shipboard bio and magentostratigraphy. This first-order estimate suggests that the meter-scale lithological cycle could correspond to the sedimentological expression of ~100-kyr short eccentricity, while the occurrence of particularly dark layers (every ~3–5 m) could represent the imprint of 405-kyr eccentricity. Vahlenkamp et al. (2020a) also observed even longer-period eccentricity expressions in their Ca/Fe series, as they employed so-called 2.4-Myr eccentricity nodes as pinpoints anchoring their floating cyclostratigraphic framework in absolute time.

These authors used a two-step tuning strategy to deal with the fact that different eccentricity solutions for the Eocene (La10a, La10b, La10c, La10d, La11) agree on the 405-kyr component, but demonstrate out-of-phase behavior at the rhythm of ~100-kyr short eccentricity. Hence, Vahlenkamp et al. (2020a) first carried out a minimal tuning to the 405-kyr component of eccentricity. In a second step, Pearson correlation coefficients were calculated to quantify the match between the tuned U1514 Eocene Ca/Fe time-series and available eccentricity reconstructions. The most powerful correlation was obtained using the La10c full eccentricity solution. Hence, this particular solution was used by Vahlenkamp et al. (2020a) to further polish their astronomical tuning.

The duration of the whole interval studied by Vahlenkamp et al. (2020a) is 16 Myr. However, in this study, we focus on a single continuous interval (140–251.715 mcd, correspond to 39.31–52.15 Ma) that contains ~31,405-kyr eccentricity cycles in the Ca/Fe time-series (Figure 6).

3.3. Sedimentary Noise Modeling Result

We modeled sedimentary noise using a 400-kyr sliding analysis window for the 33.93–41.41 Ma interval (correspond to 180–289.75 m) and 50.23–55.51 Ma interval (correspond to 332.18–412.78 m) of Hole 762C, and for the 39.31–52.15 Ma interval (correspond to 140–251.715 m) of U1514. DYNOT, and ρ_1 modeling show mirrored patterns, with fluctuating noise throughout the entire Eocene intervals of both studied sites. To evaluate a possible relationship between the Eastern Indian Ocean DYNOT results and four GSLC estimates (Haq et al., 1987; Kominz et al., 2008; Miller et al., 2005, 2020) (Figure 7), we calculated Pearson correlation coefficients between each DYNOT series and all four GSLC, using the "surrogateCor" method that has been specifically designed for serially correlated stratigraphic series (Baddouh et al., 2016) (Table 1).

For 33.93–41.41 Ma interval of Hole 762C, the DYNOT result has a strong negative correlation with Miller20 GSLC (>99% confidence level). For the 50.23–55.51 Ma interval of Hole 762C, the DYNOT result does not correlate with any of the four GSLC. For the 39.31–52.15 Ma interval of U1514, the DYNOT result correlates best with the Miller20 and Kominz GSLC (99% confidence), albeit with a positive correlation coefficient.

Previous work has shown that Eocene GSLC was largely influenced by ~1.2 Myr obliquity cycles (e.g., Boulila et al., 2011). Here, we test this proposed astronomical driver by means of spectral analysis of the

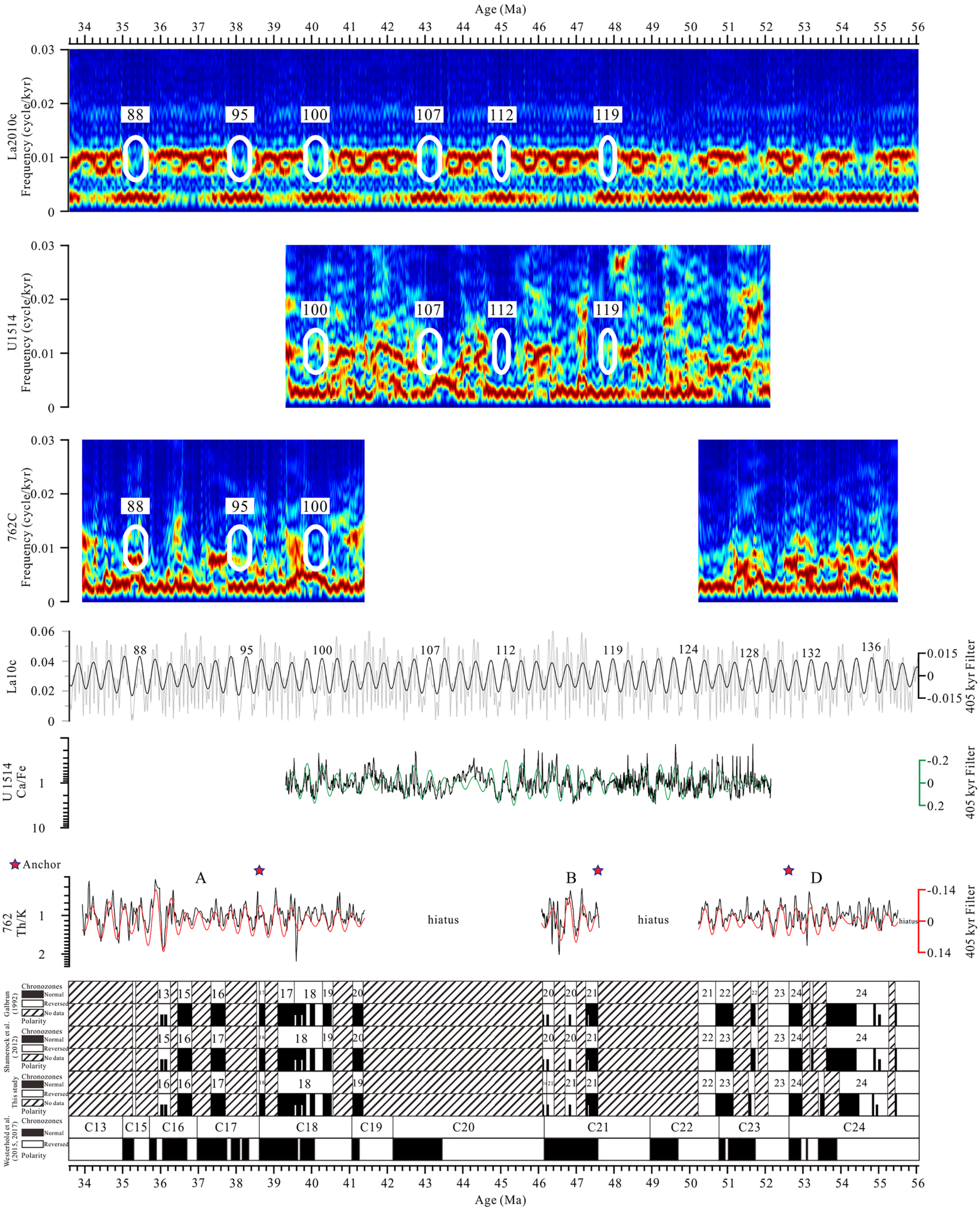
Age (Ma)
La2010c
Frequency (cycle/kyr)
88
95
100
107
112
119
U1514
762C
La10c
405 kyr Filter
124
128
132
136
U 1514
Ca/Fe
Anchor
A
B
D
762
Th/K
hiatus
Chronozones
Normal
Reversed
No data
Polarity
Galbrun (1992)
Shamrock et al. (2012)
This study
Westerhold et al. (2015, 2017)
C13
C15
C16
C17
C18
C19
C20
C21
C22
C23
C24

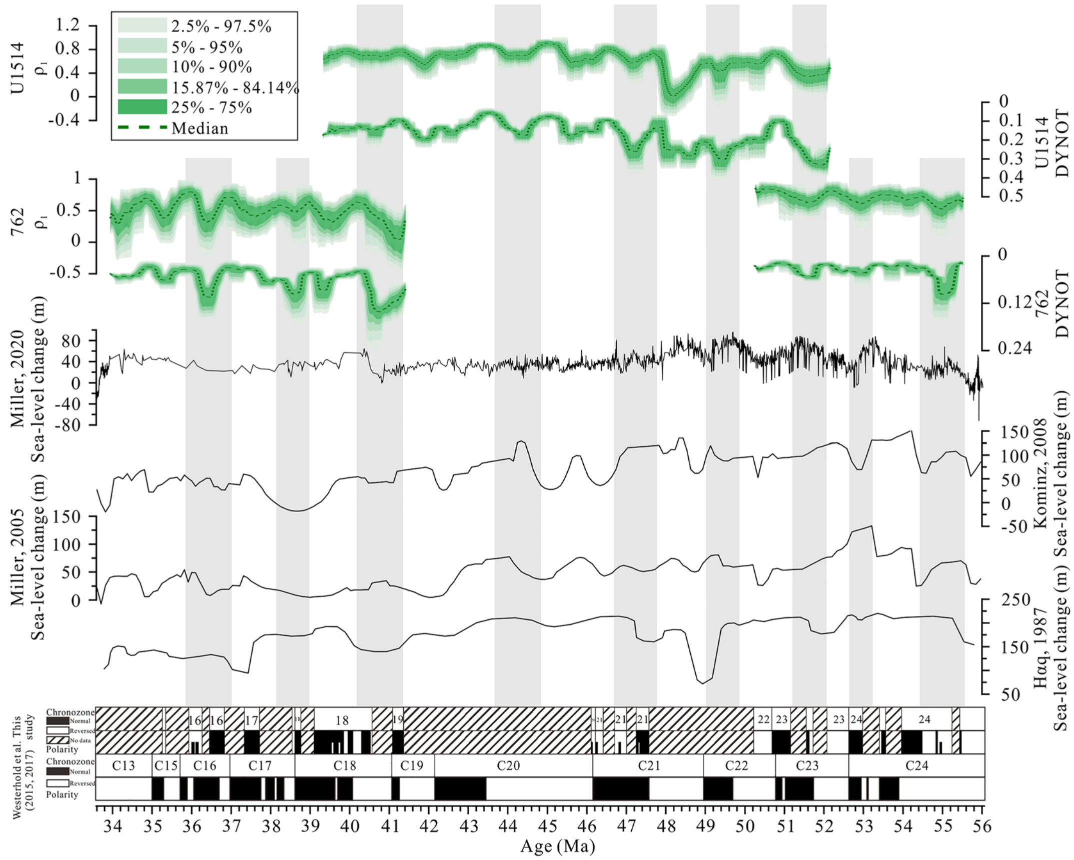

Figure 7. ρ_1 and DYNOT models of tuned Th/K time-series of Hole 762C and tuned Ca/Fe time-series of U1514 compared with Global sea levels of Haq et al. (1987), Miller et al.(2005), Kominz et al. (2008), and Miller et al. (2020). The gray columns identify co-occurring low values of ρ_1 and high values of DYNOT. DYNOT, dynamic noise after orbital tuning analysis.

Table 1
Correlation Coefficients Between the DYNOT Results in the Eastern Indian Ocean and Four GSLC

	Haq87 GSLC	Miller05 GSLC	Kominz GSLC	Miller20 GSLC
33.93–41.41 Ma interval of Hole 762C	r = 0.138 P value = 0.629	r = −0.114 P value = 0.656	r = −0.077 P value = 0.795	**r = −0.592** P value < 0.01
50.23–55.51 Ma interval of Hole 762C	r = 0.015 P value = 0.959	r = −0.027 P value = 0.897	r = −0.234 P value = 0.408	r = −0.107 P value = 0.601
39.31–52.15 Ma interval of U1514	r = −0.122 P value = 0.514	r = 0.29 P value = 0.448	**r = 0.532** P value = 0.01	**r = 0.534** P value = 0.01

Abbreviations: DYNOT, dynamic noise after orbital tuning analysis; GSLC, global sea-level change.
Note. Values in bold represent statistically significant correlation coefficients and are discussed in the main text

DYNOT and ρ_1 results (Figure 8). All power spectra show a main cycle in sedimentary noise with a period of ~1.2 Myr and with high F-test significance values at this frequency. We then calculated Pearson correlation coefficients (again using surrogateCor) between the 1.2-Myr filter of Miller20 GSLC and the 1.2-Myr filter of the DYNOT reconstructions. As expected from the face-value correlation assessment for Site 762,

Figure 6. Comparison of different magnetostratigraphic interpretations of at Hole 762C and the magnetostratigraphy based on the age model of Westerhold et al. (2015, 2017). Astronomical time scale (ATS) for the composite Eocene succession (Hole 762C and U1514) in the Eastern Indian Ocean. The La2010c eccentricity solution during Eocene. Evolutionary FFT spectrogram of the Hole 762C, U1514, La2010c eccentricity time-series (sliding window is 500 kyr with a step of 10 kyr). White ovals in evolutionary FFT spectrogram represent the 2.4-Myr eccentricity nodes; the numbers on the eccentricity cycles indicate the position of the 2.4-Myr eccentricity nodes. The red stars represent the anchor point. A represent the timeseries of 762C of 180–289.75 mbsf interval, B represent the timeseries of 762C of 289.75–321.13 mbsf interval, D represent the timeseries of 762C of 332.18–412.78 mbsf interval. FFT, Fast Fourier transform.

10.1029/2020PA004116

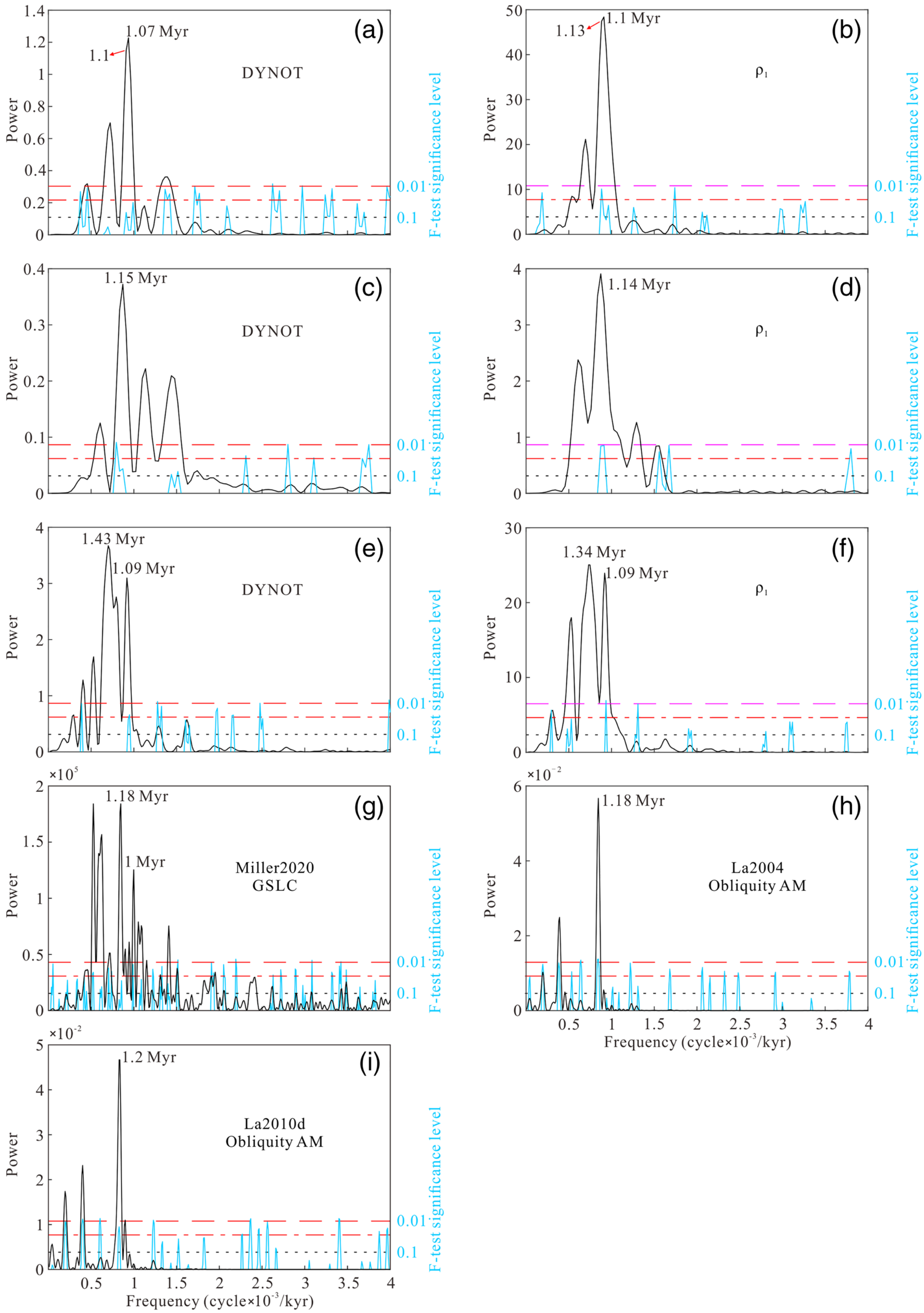

Figure 8. Periodograms (black) and F-test significance values (blue) of detrended median output from DYNOT and ρ_1 models. (a–b) Hole 762C of 180–289.75 mbsf interval. (c–d) Hole 762C of 332.18–412.78 mbsf interval. (e–f) U1514 of 140–251.715 mcd interval. (g) Periodograms (black) and F-test significance values (blue) of the Miller2020 GSLC. (h–i) Periodograms (black) and F-test significance values (blue) of obliquity amplitude modulation (AM) in La2004 and La2010d astronomical models from 33.586 Ma to 56.056 Ma. DYNOT, dynamic noise after orbital tuning analysis.

Table 2
Key Eocene Nanno fossil Biomarkers Identified in Hole 762C (Shamrock et al., 2012)

Biostratigraphy	Samples	Occurrence	Depth (msbf)	This study (Ma)	GTS2012 (Ma)	Difference (Myr)
Discoaster barbadiensis	762C-3-1-49	LO	184.49	34.25	34.76	0.51
Discoaster saipanensis	762C-3-1-49	LO	184.49	34.25	34.44	0.19
Reticulofenestra oamaruensis	762C-3-1-49	LO	184.49	34.25	33.97	−0.28
Chiasmolithus oamaruensis	762C-8-5-50	FO	233.5	37.72	38.09	0.37
Chiasmolithus solitus	762C-12-3-125	LO	270	39.95	40.4	0.45
Discoaster sublodoensis	762C-15-3-48	LO	296.98	46.41	46.21	−0.2
Sphenolithus radians	762C-25-4-125	FO	394.25	54.45	54.17	−0.28
Tribrachiatus orthostylus	762C-25-4-125	FO	394.25	54.45	54.37	−0.08
Tribrachiatus contortus	762C-26-1-49	LO	398.3	54.7	54.17	−0.53
Campylosphaera eodela	762C-28-1-59	FO	412.57	55.5	55.81	0.31
Discoaster diastypus	762C-28-1-59	FO	412.57	55.5	54.95	−0.55

Abbreviation: LO, last occurrence; FO, first occurrence.

this correlation analysis with bandpass filtered signals also indicates an antiphased relationship, albeit with lower statistical significance (33.93–41.41 Ma: $r = -0.462$, P value = 0.011; 50.23–55.51 Ma: $r = -0.38$, P value = 0.506). For the 39.31–52.15 Ma interval of U1514, the 1.2-Myr filter of the DYNOT reconstruction does not exhibit a significant correlation with the 1.2-Myr filter of Miller20 GSLC ($r = 0.091$, P value = 0.718).

4. Discussion

4.1. An ATS for Eocene Formations in the Eastern Indian Ocean

Our work provides a detailed Eocene time-depth framework for ODP Hole 762C, building on the fundamental bio and magnetostratigraphic synthesis by Shamrock et al. (2012). Table 2 indicates the depths and tuned ages for different biostratigraphic markers observed in Hole 762C. This table demonstrates that our ATS matches reasonably well with the numerical ages of biostratigraphic events in GTS2012: Seven out of 11 biostratigraphic events agree within a 405-kyr eccentricity cycle offset, while the time-offsets of the remaining four biostratigraphic time-markers do not exceed 0.56 Myr.

Based on the Hole 762C ATS, we needed to adopt a minor revision of the magnetostratigraphic interpretation by Shamrock et al. (2012) (Figure 6). Our ATS suggests that the C15 Chron of Shamrock et al. (2012) is slightly older than previously thought and actually corresponds to Chron C16. The C18r/C19n chron boundary in Shamrock et al. (2012) is placed at 273.8 mbsf. However, this level in our cyclostratigraphic age model corresponds to 40.296 Ma and therewith occurs within chron C18r. We reinterpret the available paleomagnetic data and place the C18r/C19n chron boundary at 284.5 mbsf, which corresponds with a tuned age of 41.085 Ma. A similar revision is proposed for the C19n/C19r chron boundary, from 276.2 mbsf to 289 mbsf, which results in a good match with the reversal age reported in Westerhold et al. (2015, 2017) (Table 3, Figure S15). The C20 and C21 chron boundaries remain uncertain in this study, as the raw paleomagnetic data is ambiguous in this interval.

Overall, our revised 762C magnetostratigraphy compares well with the magnetostratigraphy based on the age models of Westerhold et al. (2015, 2017). The most important offset occurs at C24n/C24r, with a time discrepancy of 0.585 Myr (Table 3). This reversal occurs in the 332.18–412.78 interval, where we opted for the C23r/C24n.1n chron boundary as the anchor point. The C24n/C24r and C23n.2n/C23r chron boundaries thus act as scrutinization points. While the tuned age of C23n.2n/C23r matches quite well with the reported ages of Westerhold et al. (2017), the C24n/C24r tuned age remains disparate (Table 3). At the same time, the tuned age for the Tribrachiatus orthostylus biomarker (394.25 msbf) is 54.45 Ma, which is quite close to the age estimate for this biomarker (54.37 Ma) in GTS2012. For these reasons, we consider our Hole

Table 3
Magnetochron Reversal Dates and Depths of This Study and the Reference Age According to Westerhold et al. (2015, 2017) and Francescone et al. (2019)

Chron boundary	Shamerock et al. (2012) base (mbsf)	This study base (mbsf)	This study (Ma)	Reference age (Ma)	Reference
C17r/C18n*	249.41	249.41	38.615	38.615	GTS2012
C18n.2n/C18r	271.6	271.6	40.078	40.076 ± 0.005	Westerhold et al. (2015)
C18r/C19n	273.8	284.5	41.085	41.061 ± 0.009	Westerhold et al. (2015)
C19n/C19r	276.2	289	41.366	41.261 ± 0.004	Westerhold et al. (2015)
C21n/C21r*	320.25	320.25	47.575	47.575 ± 0.018	Westerhold et al. (2015)
C22r/C23n	339.53	339.53	50.683	50.777 ± 0.01	Westerhold et al. (2017)
C23n/C23r	352.22	352.22	51.626	51.737 ± 0.123, 51.724	Westerhold et al. (2017); Francescone et al. (2019)
C23r/C24n*	368.31	368.31	52.628	52.628 ± 0.053 52.540	Westerhold et al. (2017); Francescone et al. (2019)
C24n/C24r	394.76	394.76	54.484	53.899 ± 0.041	Westerhold et al. (2017)

Notes. Three magnetostratigraphic reversals (indicated by *) have been used as time anchors in this study. These reversals have been assigned the reference reversal age of GTS2012, Westerhold et al. (2015, 2017), respectively. All other reversal ages reported in this study are the result of our cyclostratigraphic age-depth model for Hole 762C.

762 astrochronology as robust in this interval despite the mismatch for C24n/C24r, and we suspect that the mismatch was caused by ambiguous paleomagnetic data.

Minima in the 2.4-Myr eccentricity cycle are often referred to as eccentricity nodes. Different eccentricity solutions are congruent in their timing, even before 50 Ma (Laskar et al, 2004, 2011; Zeebe, 2017). During eccentricity nodes, 405-kyr eccentricity cycles are particularly well-expressed with elevated amplitudes, while the ~100-kyr short eccentricity amplitudes are diminished. These eccentricity nodes are imprinted in the $\log_{10}$(Th/K) time series of Hole 762C, and the Ca/Fe time series of U1514, expressed as long-lasting maxima over several hundreds of thousands of years. In the evolutionary FFT spectrograms of the tuned $\log_{10}$(Th/K) and Ca/Fe time series, eccentricity nodes can be recognized by looking for the simultaneous occurrence of high power in the 405-kyr eccentricity band and low power in the 100-kyr eccentricity band. White circles on Figure 6 indicate the points in time at which eccentricity nodes occur in the eccentricity solution, as well as in the studied proxy series. In this study, we identified the possible position of nodes in the ~2.4 Myr eccentricity cycle before 50 Ma: $\sim_{ecc}$88, $\sim_{ecc}$95 and $\sim_{ecc}$100 in $\log_{10}$(Th/K) time series of Hole 762C, $\sim_{ecc}$100, $\sim_{ecc}$107, $\sim_{ecc}$112 and $\sim_{ecc}$119 in Ca/Fe time series of U1514 (Figure 6, white circles on the evolutionary FFT spectrogram). Prior to 50 Ma, in 762C interval D, an eccentricity node at $\sim_{ecc}$132 might be discerned by a reduction in 100-kyr eccentricity power. However, its expression is less clear as the nodes in the younger interval. In fact, similar more cryptic expressions can be noted for $\sim_{ecc}$88 in the $\log_{10}$(Th/K) time series of Hole 762C and $\sim_{ecc}$100 in Ca/Fe time series of U1514. Nevertheless, the other 2.4-Myr eccentricity nodes identified in this study are unambiguous. This in turn provides support for the Eocene chronology constructed in this work.

4.2. Evaluation of Sedimentary Noise Modeling

The 762C DYNOT results are antiphased with the Miller20 GSLC, including the embedded 1.2-Myr cycles. The sedimentary noise in the Site 762 $\log_{10}$(Th/K) time-series is composed of sea-level-related noise, proxy-related noise, unstable sedimentation, short-term tectonic activity, volcanism and postdepositional diagenesis (Li et al., 2018). The proxy-related noise includes proxy sensitivity, measurement error and dating error. We estimate that all three factors are relatively minor: (1) The astronomical imprint in the $\log_{10}$(Th/K) series is rather constant throughout the studied interval, suggesting continual proxy sensitivity; (2) the analyzed proxy series has been obtained by downhole wireline logging in a stable hole, providing good and consistent measurement conditions; (3) the ATS is robust as it abides by magneto- and biostratigraphic constraints and contains indications of eccentricity nodes at the expected timings. Therefore, we assume that proxy sensitivity, measurement error and dating error exerted little influence on the total noise level. Unstable sedimentation, from short-term tectonic activity, may lead to elevated noise at all frequencies (Li et al., 2018). However, the Exmouth Plateau has been relatively quiescent since the mid-Cretaceous. Also, there is no sedimentological evidence, nor published reports that suggest nearby volcanic activity during the Paleogene. Hence, the sedimentary noise model is assumed to be largely unaffected by unstable sedimentation and volcanism. Postdepositional clay mineral diagenesis could also be a source for noise-level variability, however, the clay mineralogy of Site 762 chiefly reflects humid-climate weathering products, only marginally affected by clay mineralogy diagenesis (Haq et al., 1990). By exclusion, the sedimentary noise modeling result is thus considered to be mainly influenced by sea-level.

Hole 762C is located on a submarine plateau at 1,360 m present-day water depth. Even though the Eocene paleo-water depth was several hundred meters shallower than it is now (Gradstein, 1992). Hence, it is likely that only the tsunami and the extreme storm-wave base reached the seafloor. Particularly in the youngest studied interval of Hole 762C, the correlation analysis suggests that sea-level change at Site 762 can be reconstructed by means of sedimentary noise modeling, with the DYNOT parameter comparing well to the recent Miller et al. (2020)'s GSLC reconstruction. Moreover, both the Hole 762C and the Miller curve carry the imprint of 1.2-Myr obliquity forcing. Li et al. (2018) hypothesized that this obliquity signature is generated through aquifer eustasy, whereby the hydrological cycle and the amount of continental water storage is significantly influenced by insolation variations. These authors advocate that this effect is sufficient to cause significant global sea-level variations during nonglacial periods. The 1.2-Myr obliquity minima are associated with reduced transport and continental storage of moisture, leading to high sea level, and vice versa. High values in the 1.2-Myr filter of Miller20 GSLC would thus correspond to long-term minima in obliquity. In the oldest studied interval of Hole 762C, the correlation between the 762C DYNOT result and the Miller20 GSLC is no longer statistically significant. Yet, that doesn't imply that this eustatic mechanism was not operational at that time. Several reasons could be responsible for the lower statistical significance in this interval: (1) Most importantly, the variance of the 762C DYNOT result is low in this interval, hampering a good assessment of correlation. (2) Both records have very different temporal data resolutions, as DYNOT is quite smooth and the Miller2020 reconstruction is at 10^4-year resolution. (3) Also, it can also not be fully excluded that age model discrepancies between the Miller2020 reconstruction and the Site 762 cyclostratigraphy compromise the accuracy of the correlation assessment.

For Site U1514, the relationship between the DYNOT result and the Miller GSLC is quite different: DYNOT results are positively correlated with the Miller20 GSLC. This means that sedimentary noise increases during periods of high eustatic sea-level, contrary to what is expected for the DYNOT method when it is applied to shelf or slope sections. However, this site is located in a deep-sea basinal environment, at 3,850 m present-day water depth. Therefore, variations in sea level and consequent variations in the vertical position of the (extreme-)storm wave base are highly unlikely to affect these abyssal depths. Instead, we hypothesize that the sedimentary noise model may be affected by changes in bottom water current intensity.

During the Eocene, Site U1514 was probably bathed by Antarctic deep waters that were exported northward that is, entering the basin from the south. This interpretation is primarily based on Eocene neodymium isotope data (ε_{Nd}) from Sites 264, 738, and 757, all within the Indian Ocean. The Eocene ε_{Nd} values observed at those sites are comparable to ε_{Nd} composition observed today in bottom waters that form along the margin of Antarctica, for example around the Wilkes Land-Adélie Coast (Lambelet et al., 2018; van de Flierdt et al., 2006). Huck et al. (2017) hypothesized that intermediate and deep waters formed in the Ross Sea region during the Eocene, which were then entrained into the Indian Ocean by means of northward-flowing deep currents (Figure 1). This deep current could have flowed north along the eastern margin of the Kerguellen Plateau (e.g., Scher et al., 2014), affecting bottom-water conditions at Site U1514 in the Mentelle Basin. We hypothesize that during astronomically forced cool conditions deep water formation around Antarctica may increase. This hypothesis is inspired by the study of astronomical forcing in deep-water circulation in the western North Atlantic during the middle Eocene by Vahlenkamp, Niezgodzki, De Vleeschouwer, Bickert, et al. (2018b), who identified obliquity as the driver of middle Eocene Northern Component Water variability. Minima in

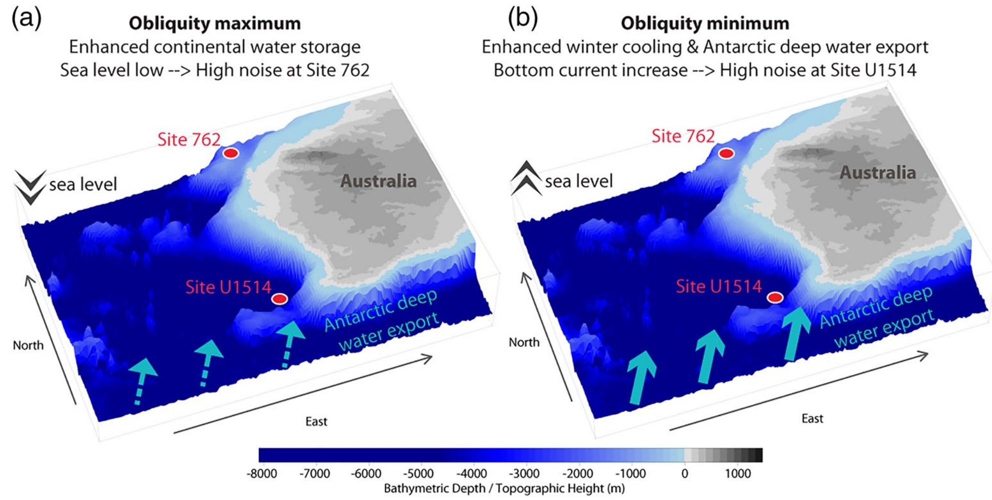

Figure 9. Visual illustration of the sedimentary noise hypothesis presented in this study. (a) During obliquity maxima, sea-level is hypothesized to be low because of enhanced continental water storage (Li et al., 2018). Hence, Hole 762C gets closer to the extreme-storm wavebase with an increase in sedimentary noise as a consequence. Low bottom current intensity because of reduced Antarctic deep water export generates low sedimentary noise at Site U1514. (b) During obliquity minima, sea-level is high and Hole 762C experiences a reduction in sedimentary noise. Antarctic deep water export increases and more intense bottom currents generate high noise levels at Site U1514. Figure made with the marmap R package (Pante & Simon-Bouhet, 2013) showcasing ETOPO1 bathymetry and topography database for the eastern Indian Ocean and Australia.

the obliquity of Earth's rotational axis could play a key role in deep water formation and export. This is because low-obliquity astronomical configurations enhance winter cooling of surface waters. Under orbitally forced warm conditions (obliquity maxima), on the other hand, deep water formation around Antarctica would be reduced (Pak & Miller, 1992). The enhanced export of Antarctic deep waters into the Indian Ocean would have contributed to stronger bottom currents, and increased sedimentary noise at Site U1514 during Eocene cool spells. This hypothesis complies with the observables, which is that the U1514 DYNOT noise result positively correlates with sea level reconstructions, under the assumption that sea-level highs are more likely to occur under obliquity minima, when less moisture is transferred to the continent and the continental storage of water in groundwater and lakes is limited (Li et al., 2018). This hypothesis also complies with the observation that the Site U1514 noise levels exhibit a 1.2-Myr cycle that can be associated with obliquity forcing (Figure 9).

5. Conclusions

Hole 762C (Exmouth Plateau, eastern Indian Ocean) provides a robust Eocene paleoceanographic archive. To correctly read this archive, we constructed an ATS based on the existing bio and magnetostratigraphies, by tuning rhythmic patterns in Th/K to 405-kyr eccentricity cycles. Our new ATS for Hole 762C matches well with the ages of key Eocene nannofossil bioevents in GTS2012 and the magnetostratigraphic timescale proposed in Westerhold et al. (2015, 2017). By combining our astrochronology with the existing astrochronology of Site U1514 from the Mentelle Basin, we constructed a regional high-resolution Eocene ATS for the Eastern Indian Ocean. The 2.4-Myr eccentricity nodes were identified in the composite Eocene record provide a robust verification of our astrochronology, and its anchoring in numerical time.

The DYNOT sedimentary noise model was applied to both sites, despite the large difference in paleo-water depth: Hole 762C represents a submarine plateau, whereas Site U1514 was deposited in a deep-sea basinal environment. Nevertheless, we find the imprint of 1.2 Myr obliquity forcing in both environments, albeit with opposite phase relationships. At Site 762, sedimentary noise is spurred when eustatic sea level is low. These sea-level low stands are hypothesized to correspond to obliquity maxima, when the hydrological cycle is enhanced and more water is stored in continental reservoirs. At Site U1514, sedimentary noise is instead thought to be associated with bottom current intensity. This would occur when the export of Antarctic deep water is maximum, for example during periods of enhanced winter cooling during obliquity minima. We thus conclude that both sites exhibit the imprint of the same astronomical parameter, however the mechanistic chains between forcing and sedimentary response are radically different.

Data Availability Statement

Site U1514 XRF-derived data are available from PANGAEA https://doi.pangaea.de/10.1594/PANGAEA.912002. Site 762 wireline NGR-derived data are available in the depth-domain from https://brg.ldeo.columbia.edu/data/odp/leg122/762C/, and in the time-domain from Supporting Data Set S1 or Zenodo https://doi.org/10.5281/zenodo.4445673.

Acknowledgments
Ke Xu is grateful to all members of the Paleoceanography Group at MARUM for hosting and adopting him during his research stay at the University of Bremen. Research data were provided by the International Ocean Discovery Program (IODP) and Ocean Drilling Program (ODP). This research was funded by the 13th 5-Year Plan's Major Science and Technology Programs of the SINOPEC (Grant No. ZDP1705) and the research stay at MARUM was financed through the Fundamental Research Funds for the Central Universities, China University of Geosciences (Wuhan). Open Access funding enabled and organized by ProjektDEAL.

References

Auer, G., De Vleeschouwer, D., & Christensen, B. A. (2020). Toward a robust plio-pleistocene chronostratigraphy for ODP Site 762. *Geophysical Research Letters*, *47*(3), e2019GL085198. https://doi.org/10.1029/2019GL085198

Baddouh, M., Meyers, S. R., Carroll, A. R., Beard, B. L., & Johnson, C. M. (2016). Lacustrine 87 Sr/86 Sr as a tracer to reconstruct Milankovitch forcing of the Eocene hydrologic cycle. *Earth and Planetary Science Letters*, *448*, 62–68. https://doi.org/10.1016/j.epsl.2016.05.007

Berggren, W. A., Kent, D. V., Swisher, C. C., III, & Aubry, M. (1995). A revised Cenozoic geochronology and chronostratigraphy. In W. A. Berggren, D. V. Kent, & M. Aubry (Eds.), *Geochronology, Time Scales and Global Stratigraphic Correlation, SEPM Society for Sedimentary Geology Special Publication*, (Vol. 54, pp. 129–212). SEPM Society for Sedimentary Geology. https://doi.org/10.2110/pec.95.04.0129

Bohaty, S. M., & Zachos, J. C. (2003). Significant Southern Ocean warming event in the late middle Eocene. *Geology*, *31*(11), 1017. https://doi.org/10.1130/G19800.1

Bohaty, S. M., Zachos, J. C., Florindo, F., & Delaney, M. L. (2009). Coupled greenhouse warming and deep-sea acidification in the middle Eocene. *Paleoceanography*, *24*(2), PA2207. https://doi.org/10.1029/2008PA001676

Boscolo Galazzo, F., Thomas, E., Pagani, M., Warren, C., Luciani, V., & Giusberti, L. (2014). The middle Eocene climatic optimum (MECO): A multiproxy record of paleoceanographic changes in the southeast Atlantic (ODP Site 1263, Walvis Ridge). *Paleoceanography*, *29*(12), 1143–1161. https://doi.org/10.1002/2014PA002670

Boulila, S., Galbrun, B., Miller, K. G., Pekar, S. F., Browning, J. V., Laskar, J., et al. (2011). On the origin of Cenozoic and Mesozoic "third-order" eustatic sequences. *Earth-Science Reviews*, *109*(3–4), 94–112. https://doi.org/10.1016/jearscirev.2011.09.003

Boulila, S., Vahlenkamp, M., De Vleeschouwer, D., Laskar, J., Yamamoto, Y., Pälike, H., et al. (2018). Towards a robust and consistent middle Eocene astronomical timescale. *Earth and Planetary Science Letters*, *486*, 94–107. https://doi.org/10.1016/j.epsl.2018.01.003

Catuneanu, O., Abreu, V., Bhattacharya, J. P., Blum, M. D., Dalrymple, R. W., Eriksson, P. G., et al. (2009). Towards the standardization of sequence stratigraphy. *Earth-Science Reviews*, *92*(1–2), 1–33. https://doi.org/10.1016/j.earscirev.2008.10.003

Cleveland, W. S. (1979). Robust locally weighted regression and smoothing scatterplots. *Journal of the American Statistical Association*, *74*(368), 829–836. https://doi.org/10.1080/01621459.1979.10481038

Coxall, H. K., & Pearson, P. N. (2007). The eocene-oligocene transition. In M. Williams, A. M. Haywood, F. J. Gregory, & D. N. Schmidt (Eds.), *Deep time perspectives on climate change: Marrying the signal from computer models and biological proxies, The Micropalaeontological Society, Special Publications*, (pp. 351–387). London: The Geological Society.

De Vleeschouwer, D., Petrick, B. F. & Martínez García, A. (2019). Stepwise weakening of the Pliocene Leeuwin current. *Geophysical Research Letters*, *46*(14), 8310–8319. https://doi.org/10.1029/2019GL083670

Dinarès-Turell, J., Martínez-Braceras, N. & Payros, A. (2018). High-resolution integrated cyclostratigraphy from the Oyambre section (Cantabria, N Iberian Peninsula): Constraints for orbital tuning and correlation of middle eocene Atlantic deep-sea records. *Geochemistry, Geophysics, Geosystems*, *19*(3), 787–806. https://doi.org/10.1002/2017GC007367

Edgar, K. M., Wilson, P. A., Sexton, P. F., Gibbs, S. J., Roberts, A. P. & Norris, R. D. (2010). New biostratigraphic, magnetostratigraphic and isotopic insights into the Middle Eocene Climatic Optimum in low latitudes. *Palaeogeography, Palaeoclimatology, Palaeoecology*, *297*(3–4), 670–682. https://doi.org/10.1016/j.palaeo.2010.09.016

Francescone, F., Lauretano, V., Bouligand, C., Moretti, M., & Galeotti, S. (2019). A 9 million-year-long astrochronological record of the early–middle Eocene corroborated by seafloor spreading rates. *The Geological Society of America Bulletin*, *131*(3–4), 499–520.

Galbrun, B. (1992). Magnetostratigraphy of upper Cretaceous and lower tertiary sediments, sites 761 and 762, Exmouth Plateau, northwest Australia. In U. von Rad, B. U. Haq, (Eds.), *Proceedings of the ocean drilling program, scientific results*. (Vol. 122, pp. 699–716). College Station, TX: Ocean Drilling Program. https://doi.org/10.2973/odp.proc.sr.122.149.1992

Ghasemi-Nejad, E., Ruffell, A., Rahimpour-Bonab, H., Sharifi, M., Soltani, B., & Sfidari, E. (2015). Spectral gamma-ray logs and palaeoclimate change? Permian-Triassic, Persian Gulf. *Geological Journal*, *50*(2), 210–219. https://doi.org/10.1002/gj.2552

Gradstein, F. M. (1992). 43. Legs 122 and 123, northwestern Australian margin—A stratigraphic and paleogeographic summary. In F. M. Gradstein, J. N. Ludden, et al. (Eds). *Proceedings of the Ocean Drilling Program, scientific reports, Leg 123*, (Vol. 123, pp. 801–816). College Station, TX: Ocean Drilling Program. https://doi.org/10.2973/odp.proc.sr.123.110.1992

Gradstein, F. M., Ogg, J. G., Schmitz, M. & Ogg, G. (2012). F. M., Gradstein, J. G., Ogg, M., Schmitz, & G., Ogg (Eds.), *The geologic time scale 2012* (p. 1176). Elsevier. https://doi.org/10.1016/C2011-1-08249-8

Groeneveld, J., Henderiks, J., Renema, W., McHugh, C. M., De Vleeschouwer, D., Christensen, B. A., et al. (2017). Australian shelf sediments reveal shifts in Miocene Southern Hemisphere westerlies. *Science Advances*, *3*(5), e1602567. https://doi.org/10.1126/sciadv.1602567

Haq, B. U., Boyd, R. L., & Exon, N. F. (1992). Evolution of the central Exmouth Plateau a post-drilling perspective. In U. von Rad, B. U. Haq, et al. (Eds.), *Proceedings of the ocean drilling program, scientific results*, (Vol. 122, pp. 801–816). College Station, TX: Ocean Drilling Program. https://doi.org/10.2973/odp.proc.sr.122.182.1992

Haq, B. U., Hardenbol, J., & Vail, P. R. (1987). Chronology of fluctuating sea levels since the triassic. *Science*, *235*(4793), 1156–1167. https://doi.org/10.1126/science.235.4793.1156

Haq, B. U., von Rad, U. & O'Connell, S. (1990). Site 762. In B. U. Haq, U. von Rad, & S. O'Connell. *Proceedings of the ocean drilling program, Initial Reports, Leg* 122, (Vol. 122, pp. 213–288). College Station, TX: Ocean Drilling Program. https://doi.org/10.2973/odp.proc.ir.122.108.1990

Hinnov, L. A. (2013). Cyclostratigraphy and its revolutionizing applications in the earth and planetary sciences. *The Geological Society of America Bulletin*, *125*(11–12), 1703–1734. https://doi.org/10.1130/B30934.1

Hinnov, L. A., & Hilgen, F. J. (2012). Cyclostratigraphy and astrochronology. In F. M. Gradstein, J. G. Ogg, M. D. Schmitz, & G. M. Ogg (Eds.), *The Geologic Time Scale 2012*, (pp. 63–83). Elsevier. https://doi.org/10.1016/B978-0-444-59425-9.00004-4

Hren, M. T., Sheldon, N. D., Grimes, S. T., Collinson, M. E., Hooker, J. J., Bugler, M., et al. (2013). Terrestrial cooling in Northern Europe during the Eocene-Oligocene transition. *Proceedings of the National Academy of Sciences*, *110*(19), 7562–7567. https://doi.org/10.1073/pnas.1210930110

Huber, B. T., Hobbs, R. W., Bogus, K. A., Batenburg, S. J., Brumsack, H. J., Guerra, R. D. M., et al. (2019). Site U1514. In R. W. Hobbs, B. T. Huber, K. A. Bogus, the Expedition 369 Scientists (Eds), Proceedings of the International Ocean Discovery Program, (Vol. 369). College Station, TX: Australia Cretaceous Climate and Tectonics. https://doi.org/10.14379/iodp.proc.369.105.2019

Huck, C. E., van de Flierdt, T., Bohaty, S. M., & Hammond, S. J. (2017). Antarctic climate, Southern Ocean circulation patterns, and deep water formation during the Eocene. *Paleoceanography*, *32*(7), 674–691. https://doi.org/10.1002/2017PA003135

Jovane, L., Sprovieri, M., Coccioni, R., Florindo, F., Marsili, A., & Laskar, J. (2010). Astronomical calibration of the middle Eocene Contessa Highway section (Gubbio, Italy). *Earth and Planetary Science Letters*, *298*(1–2), 77–88. https://doi.org/10.1016/j.epsl.2010.07.027

Keery, J. S., Holden, P. B., & Edwards, N. R. (2018). Sensitivity of the Eocene climate to CO_2 and orbital variability. *Climate of the Past*, *14*(2), 215–238. https://doi.org/10.5194/cp-14-215-2018

Kodama, K. P., Anastasio, D. J., Newton, M. L., Pares, J. M., & Hinnov, L. A. (2010). High-resolution rock magnetic cyclostratigraphy in an Eocene flysch, Spanish Pyrenees. *Geochemistry, Geophysics, Geosystems*, *11*(6). https://doi.org/10.1029/2010GC003069

Kodama, K. P., & Hinnov, L. A. (2014). *Rock magnetic cyclostratigraphy*, New Analytical Methods in Earth and Environmental Science, (p. 1–144). Oxford: Wiley-Blackwell. https://doi.org/10.1002/9781118561294

Kominz, M. A., Browning, J. V., Miller, K. G., Sugarman, P. J., Mizintseva, S., & Scotese, C. R. (2008). Late Cretaceous to Miocene sea-level estimates from the New Jersey and Delaware coastal plain coreholes: An error analysis. *Basin Research*, *20*(2), 211–226. https://doi.org/10.1111/j.1365-2117.2008.00354.x

Kuhnt, W., Holbourn, A., Xu, J., Opdyke, B., De Deckker, P., Röhl, U., et al. (2015). Southern Hemisphere control on Australian monsoon variability during the late deglaciation and Holocene. *Nature Communications*, *6*(1), 5916. https://doi.org/10.1038/ncomms6916

Lambelet, M., Flierdt, T., Butler, E. C. V., Bowie, A. R., Rintoul, S. R., Watson, R. J., et al. (2018). The Neodymium isotope fingerprint of Adélie Coast bottom water. *Geophysical Research Letters*, *45*(20), 11,247–11,256. https://doi.org/10.1029/2018GL080074

Laskar, J., Fienga, A., Gastineau, M., & Manche, H. (2011). La2010: A new orbital solution for the long term motion of the Earth. *Astronomy & Astrophysics*, *532*(2), 784–785. https://doi.org/10.1051/0004-6361/201116836

Laskar, J., Robutel, P., Joutel, F., Gastineau, M., Correia, A. C. M., & Levrard, B. (2004). A long-term numerical solution for the insolation quantities of the Earth. *Astronomy & Astrophysics*, *428*(1), 261–285. https://doi.org/10.1051/0004-6361:20041335

Li, M., Hinnov, L. A., Huang, C., & Ogg, J. G. (2018). Sedimentary noise and sea levels linked to land–ocean water exchange and obliquity forcing. *Nature Communications*, *9*(1), 1004. https://doi.org/10.1038/s41467-018-03454-y

Li, M., Hinnov, L., & Kump, L. (2019). Acycle: Time-series analysis software for paleoclimate research and education. *Computers & Geosciences, 127*, 12–22. https://doi.org/10.1016/j.cageo.2019.02.011

Li, M., Huang, C., Ogg, J., Zhang, Y., Hinnov, L., Wu, H., et al. (2019). Paleoclimate proxies for cyclostratigraphy: Comparative analysis using a Lower Triassic marine section in South China. *Earth-Science Reviews*, *189*, 125–146. https://doi.org/10.1016/j.earscirev.2019.01.011

Lourens, L. J., Sluijs, A., Kroon, D., Zachos, J. C., Thomas, E., Röhl, U., et al. (2005). Astronomical pacing of late Palaeocene to early Eocene global warming events. *Nature*, *435*(7045), 1083–1087. https://doi.org/10.1038/nature03814

Lunt, D. J., Bragg, F., Chan, W., Hutchinson, D. K., Ladant, J., Niezgodzki, I., et al. (2020). DeepMIP: Model intercomparison of early Eocene climatic optimum (EECO) large-scale climate features and comparison with proxy data. *Climate of the Past*, *17*, 203–227.

Mann, M. E., & Lees, J. M. (1996). Robust estimation of background noise and signal detection in climatic time series. *Climatic Change*, *33*(3), 409–445. https://doi.org/10.1007/BF00142586

Miller, K. G., Browning, J. V., Schmelz, W. J., Kopp, R. E., Mountain, G. S., & Wright, J. D. (2020). Cenozoic sea-level and cryospheric evolution from deep-sea geochemical and continental margin records. *Science Advances*, *6*(20), eaaz1346. https://doi.org/10.1126/sciadv.aaz1346

Miller, K. G., Kominz, M. A., Browning, J. V., Wright, J. D., Mountain, G. S., Katz, M. E., et al. (2005). The Phanerozoic record of global sea-level change. *Science*, *310*(5752), 1293–1298. https://doi.org/10.1126/science.1116412

Norris, R. D., & Röhl, U. (1999). Carbon cycling and chronology of climate warming during the Palaeocene/Eocene transition. *Nature*, *401*(6755), 775–778. https://doi.org/10.1038/44545

Pak, D. K., & Miller, K. G. (1992). Paleocene to Eocene benthic foraminiferal isotopes and assemblages: Implications for deepwater circulation. *Paleoceanography*, *7*(4), 405–422. https://doi.org/10.1029/92PA01234

Pälike, H., Shackleton, N. J., & Röhl, U. (2001). Astronomical forcing in Late Eocene marine sediments. *Earth and Planetary Science Letters*, *193*(3), 589–602. https://doi.org/10.1016/S0012-821X(01)00501-5

Pante, E., & Simon-Bouhet, B. (2013). Marmap: A package for importing, plotting and analyzing bathymetric and topographic data in R. *PloS One*, *8*(9), e73051. https://doi.org/10.1371/journal.pone.0073051

Scher, H. D., Bohaty, S. M., Smith, B. W., & Munn, G. H. (2014). Isotopic interrogation of a suspected late Eocene glaciation. *Paleoceanography*, *29*(6), 628–644. https://doi.org/10.1002/2014PA002648

Schnyder, J., Ruffell, A., Deconinck, J., & Baudin, F. (2006). Conjunctive use of spectral gamma-ray logs and clay mineralogy in defining late Jurassic–early Cretaceous palaeoclimate change (Dorset, U.K.). *Palaeogeography, Palaeoclimatology, Palaeoecology*, *229*(4), 303–320. https://doi.org/10.1016/j.palaeo.2005.06.027

Shamrock, J. L., & Watkins, D. K. (2012). Eocene calcareous nannofossil biostratigraphy and community structure from Exmouth Plateau, Eastern Indian Ocean (ODPSite 762). *Stratigraphy*, *9*(1), 1–54.

Shamrock, J. L., Watkins, D. K., & Johnston, K. W. (2012). Eocene biogeochronology and magnetostratigraphic revision of ODP Hole 762C, Exmouth Plateau (northwest Australian Shelf). *Stratigraphy*, *9*(1), 55–75.

Siesser, W. G., & Bralower, T. J. (1992). Cenozoic calcareous nannofossil biostratigraphy on the Exmouth Plateau, Eastern Indian Ocean. In U. von Rad, B. U. Haq, et al. (Eds.), *Proceedings of the ocean drilling program, scientific results*, (Vol. 122, pp. 601–631). College Station, TX: Ocean Drilling Program. https://doi.org/10.2973/odp.proc.sr.122.162.1992

Sluijs, A., Zeebe, R. E., Bijl, P. K., & Bohaty, S. M. (2013). A middle Eocene carbon cycle conundrum. *Nature Geoscience*, *6*(6), 429–434. https://doi.org/10.1038/ngeo1807

Strasser, A., Hilgen, F. J., & Heckel, P. H. (2006). Cyclostratigraphy—Concepts, definitions, and applications. *Newsletters on Stratigraphy*, *42*(2), 75–114. https://doi.org/10.1127/0078-0421/2006/0042-0075

Stuut, J. B. W., De Deckker, P., Saavedra Pellitero, M., Bassinot, F., Drury, A. J., Walczak, M. H., et al. (2019). A 5.3-million-year history of monsoonal precipitation in Northwestern Australia. *Geophysical Research Letters*, *46*(12), 6946–6954. https://doi.org/10.1029/2019GL083035

Thomas, E., Shackleton, N. J., & Hall, M. A. (1992). Data report: Carbon isotope stratigraphy of Paleogene bulk sediments, Hole 762C (Exmouth Plateau, eastern Indian Ocean). In U. von Rad, B. U. Haq, et al. (Eds.), *Proceedings of ocean drilling program, scientific results*, (Vol. 122, pp. 897–901). College Station, TX: Ocean Drilling Program. https://doi.org/10.2973/odp.proc.sr.122.195.1992

Thomson, D. J. (1982). Spectrum estimation and harmonic analysis. *Proceedings of the IEEE*, *70*(9), 1055–1096. https://doi.org/10.1109/PROC.1982.12433

Tripati, A., & Elderfield, H. (2005), Deep-sea temperature and circulation changes at the Paleocene-Eocene thermal maximum. *Science*, *308*(5730), 1894–1898. https://doi.org/10.1126/science.1109202

Vahlenkamp, M., De Vleeschouwer, D., Batenburg, S. J., Edgar, K. M., Hanson, C. E., Martinez, M., et al. (2020b). Bulk stable isotopes of IODP Site 369-U1514. *PANGAEA*. https://doi.org/10.1594/PANGAEA.911998

Vahlenkamp, M., De Vleeschouwer, D., Batenburg, S. J., Edgar, K. M., Hanson, C. E., Martinez, M., et al. (2020a). A lower to middle Eocene astrochronology for the Mentelle Basin (Australia) and its implications for the geologic time scale. *Earth and Planetary Science Letters*, *529*, 115865. https://doi.org/10.1016/j.epsl.2019.115865

Vahlenkamp, M., Niezgodzki, I., De Vleeschouwer, D., Bickert, T., Harper, D., Kirtland Turner, S., et al. (2018a). Astronomically paced changes in deep-water circulation in the western North Atlantic during the middle Eocene. *Earth and Planetary Science Letters*, *484*, 329–340. https://doi.org/10.1016/j.epsl.2017.12.016

Vahlenkamp, M., Niezgodzki, I., De Vleeschouwer, D., Lohmann, G., Bickert, T., & Pälike, H. (2018b). Ocean and climate response to North Atlantic seaway changes at the onset of long-term Eocene cooling. *Earth and Planetary Science Letters*, *498*, 185–195. https://doi.org/10.1016/j.epsl.2018.06.031

Vail, P. R., Mitchum, R. M., Jr., & Thompson, S., III (1977). Seismic stratigraphy and global changes of sea level: Part 3. Relative changes of sea level from coastal onlap: Section 2. Application of Seismic Reflection Configuration to Stratigrapic Interpretation. In C. E. Payton, *Seismic Stratigraphy—Applications to Hydrocarbon Exploration*, (Vol. 26, pp. 63–81). Tulsa, USA: American Association of Petroleum Geologists Memoir.

van de Flierdt, T., Hemming, S. R., Goldstein, S. L., & Abouchami, W. (2006). Radiogenic isotope fingerprint of Wilkes Land–Adélie coast bottom water in the circum-Antarctic Ocean. *Geophysical Research Letters*, *33*(12), L12606. https://doi.org/10.1029/2006GL026020

Weedon, G. P. (Ed.) (2003). *Time-series analysis and cyclostratigraphy: Examining stratigraphic records of environmental cycles*. (p. 259). Cambridge, UK: Cambridge University Press. https://doi.org/10.1017/CBO9780511535482

Westerhold, T., & Röhl, U. (2009). High resolution cyclostratigraphy of the early Eocene—New insights into the origin of the Cenozoic cooling trend. *Climate of the Past*. 309–327. https://doi.org/10.5194/cp-5-309-2009

Westerhold, T., & Röhl, U. (2013). Orbital pacing of Eocene climate during the middle Eocene climate optimum and the chron C19r event: Missing link found in the tropical western Atlantic. *Geochemistry, Geophysics, Geosystems*, *14*(11), 4811–4825. https://doi.org/10.1002/ggge.20293

Westerhold, T., Röhl, U., Frederichs, T., Agnini, C., Raffi, I., Zachos, J. C., et al. (2017). Astronomical calibration of the Ypresian timescale: Implications for seafloor spreading rates and the chaotic behavior of the solar system? *Climate of the Past*, *13*(9), 1129–1152. https://doi.org/10.5194/cp-13-1129-2017

Westerhold, T., Röhl, U., Frederichs, T., Bohaty, S. M., & Zachos, J. C. (2015). Astronomical calibration of the geological timescale: Closing the middle Eocene gap. *Climate of the Past*, *11*(9), 1181–1195. https://doi.org/10.5194/cp-11-1181-2015

Westerhold, T., Röhl, U., Laskar, J., Raffi, I., Bowles, J., Lourens, L. J., et al. (2007). On the duration of magnetochrons C24r and C25n and the timing of early Eocene global warming events: Implications from the Ocean Drilling Program Leg 208 Walvis Ridge depth transect. *Paleoceanography*, *22*(2), PA2201. https://doi.org/10.1029/2006PA001322

Westerhold, T., Röhl, U., Pälike, H., Wilkens, R., Wilson, P. A., & Acton, G. (2014). Orbitally tuned timescale and astronomical forcing in the middle Eocene to early Oligocene. *Climate of the Past*, *10*(3), 955–973. https://doi.org/10.5194/cp-10-955-2014

Zachos, J. C., Dickens, G. R., & Zeebe, R. E. (2008). An early Cenozoic perspective on greenhouse warming and carbon-cycle dynamics. *Nature*, *451*(7176), 279–283. https://doi.org/10.1038/nature06588

Zachos, J. C., Pagani, M., Sloan, L., Thomas, E., & Billups, K. (2001). Trends, rhythms, and aberrations in global climate 65 Ma to present. *Science*, *292*(5517), 686–693. https://doi.org/10.1126/science.1059412

Zeebe, R. E. (2017). Numerical solutions for the orbital motion of the solar system over the past 100 Myr: Limits and new results. *The Astronomical Journal*, *154*(5), 193. https://doi.org/10.3847/1538-3881/aa8cce

Zeebe, R. E., & Lourens, L. J. (2019). Solar System chaos and the Paleocene-Eocene boundary age constrained by geology and astronomy. *Science*, *365*(6456), 926–929. https://doi.org/10.1126/science.aax0612